

# PCCP

Accepted Manuscript



This is an *Accepted Manuscript*, which has been through the Royal Society of Chemistry peer review process and has been accepted for publication.

*Accepted Manuscripts* are published online shortly after acceptance, before technical editing, formatting and proof reading. Using this free service, authors can make their results available to the community, in citable form, before we publish the edited article. We will replace this *Accepted Manuscript* with the edited and formatted *Advance Article* as soon as it is available.

You can find more information about *Accepted Manuscripts* in the [Information for Authors](#).

Please note that technical editing may introduce minor changes to the text and/or graphics, which may alter content. The journal's standard [Terms & Conditions](#) and the [Ethical guidelines](#) still apply. In no event shall the Royal Society of Chemistry be held responsible for any errors or omissions in this *Accepted Manuscript* or any consequences arising from the use of any information it contains.

# Conceptual design of the tetraazaporphyrin- and subtetraazaporphyrin-based functional nanocarbon materials: electronic structures, topologies, optical properties, and methane storage capacities

*Rodion V. Belosludov,<sup>a\*</sup> Hannah M. Rhoda,<sup>b</sup> Ravil K. Zhdanov<sup>c</sup> Vladimir R. Belosludov,<sup>c</sup> Yoshiyuki Kawazoe,<sup>d</sup> Victor N. Nemykin<sup>b\*</sup>*

<sup>a</sup> Institute for Materials Research, Tohoku University, Sendai, 980-85577, Japan

<sup>b</sup> Department of Chemistry and Biochemistry, University of Minnesota Duluth, Duluth, Minnesota, 55812, USA.

<sup>c</sup> Nikolaev Institute of Inorganic Chemistry, SB RAS, Lavrentiev 3, Novosibirsk, 630090, Russia

<sup>d</sup> New Industry Creation Hatchery Center, Tohoku University, 6-6-4 Aoba, Aramaki, Sendai – 980-8579, Japan.

## KEYWORDS

Phthalocyanine, tetraazaporphyrin, subtetraazaporphyrin, subphthalocyanine, DFT, TDDFT, nanocage, nanobarrel, nanotube, methane adsorption

## ABSTRACT

A large variety of the conceptual three- and four-fold tetraazaporphyrin- and subtetraazaporphyrin-based functional 3D nanocage and nanobarrel structures have been proposed on the basis of *in silico* design. Designed structures differ by their sizes, topology, porosity, and conjugation properties. The stability of the  $O_h$  symmetry nanocages and the  $D_{4h}$  symmetry nanobarrels was elucidated on the basis of DFT and MD calculations while the optical properties were accessed using the TDDFT approach and a long-range corrected LC-wPBE exchange-correlation functional. It was shown that the electronic structures and vertical excitation energies of the functional nanocage and nanobarrel structures could be easily tuned up by their size, topology, and the presence of bridging  $sp^3$  carbon atoms. TDDFT calculations suggest significantly lower excitation energies in fully conjugated nanocages and nanobarrels compared to the systems with bridging  $sp^3$  carbon fragments. Based on DFT and TDDFT calculations, the optical properties of the new materials can be rival to known quantum dots and superior to monomeric phthalocyanines and their analogues. Methane gas adsorption properties of the new nano-structures and generated by translation from nanobarrels nanotubes were studied using the MD simulation approach. The ability to store large methane quantities ( $106 - 216 \text{ cm}^3 \text{ (STP)/cm}^3$ ) was observed in all cases with several compounds being close or exceeding the DOE target of  $180 \text{ cm}^3 \text{ (STP) / cm}^3$  for material-based methane storage at 3.5 MPa pressure and room temperature.

## **Introduction.**

During the last several decades, the fundamental research and technological activities in the field of nanoscience grew in tremendous ways.<sup>[1]</sup> Nowadays it is commonly accepted that design and preparation of the uniform nanomaterials with specific 1D, 2D, or 3D topology useful for high-performance nanoscale-size electronic, optical, magnetic, mechanical, and biomedical devices is one of the main challenges in nanotechnology and nanofabrication.<sup>[2]</sup> The search for thermally and chemically robust structures, with well-ordered molecular-scale architecture, requires an access to complex mono-disperse building blocks with desired topology and size.

Carbon-based materials, such as fullerenes,<sup>[3]</sup> carbon nanotubes,<sup>[4]</sup> and graphene<sup>[5]</sup> are very exciting molecular-level building blocks for nanoscale materials design. A large number of accessible hybridizations of the carbon atom allows the construction of a variety of basic 1D, 2D, and 3D shapes and geometries needed to build any specifically designed molecular architecture.<sup>[6]</sup> However, the separation of a synthetic mixture of the major and minor products into mono-disperse or single chirality components, especially in the case of carbon nanotubes, is still a big challenge for researchers and hence provides some limitations to access the pure carbon nano-materials for technological applications. Therefore, design of an alternative to the solely carbon-based nano-materials with specific structural topologies has sparked a lot of scientific interest in the last several decades. In general, two main groups of building blocks emerged the field of the alternative to nano-carbon materials.

The first general group of nano-composites consists of well-defined inorganic compounds and clusters. Good examples of such materials are inorganic boron nitride-based (BN) nanostructures which can mimic all basic architectures that are available for carbon nano-materials.<sup>[7-9]</sup> Another example of inorganic nano-materials is represented by a number of binary semiconducting

clusters. For instance, preparation and characterization of the small fullerene-like core-shell nanoclusters of general formula  $(\text{CdSe})_n$  ( $n = 13, 33, \text{ and } 34$ ) was recently a subject for intensive experimental and theoretical studies.<sup>[10]</sup> It was found that these puckered cage-like nano-clusters are energetically more favorable as compared to the crystalline CdSe bulk fragment and similar trends were also found for CdS, CdTe, ZnS, and ZnSe nano-clusters.<sup>[11]</sup> These inorganic building blocks provide the possibility to design novel artificial materials with higher complexity and improved functionality as compared to the solely pure carbon-based nanostructures.

The second large group of the nano-scale materials, which can be rival to the pure nanocarbon-based systems, belongs to organic supramolecular assemblies, which consist of covalently or non-covalently bounded functional monomeric building blocks. One of the most interesting building blocks for such organic supramolecular assemblies is porphyrins, and related to them, phthalocyanines.<sup>[12]</sup> These thermally and chemically robust platforms found a variety of applications ranging from traditional dyes and pigments to more contemporary photodynamic- and boron-neutron capture cancer therapies, optical limiting, environmental and biochemical sensors, nonlinear optics, nanotechnology, and light-harvesting.<sup>[13-16]</sup> Such a variety of applications reflect the easiness to tune optical, magnetic, and redox properties of porphyrins, phthalocyanines, and their analogues by varying their degree of conjugation, electron-donating or electron-withdrawing strength of substituents, and the nature of the central metal residing in macrocyclic cavity. For instance, the transformation of tetraazaporphyrins to phthalocyanines to naphthalocyanines to antraphthalocyanines results in an incremental  $\sim 100$  nm low-energy shift of the intense low-energy  $Q$ -band for each additional conjugated benzene fragment.<sup>[17]</sup> Similarly, the stability towards oxidation in this series is also stepwise reduced with conjugation of each additional benzene fragment, which reflects the destabilization of the HOMO orbital in these

macrocycles. Recently developed for porphyrins and phthalocyanines, synthetic methodologies allowed the creation of fully conjugated graphene-like phthalocyanine 2D structures on electroactive surfaces. In addition, Osuka and co-workers as well as the other research groups reported several fused or covalently linked porphyrin systems with well-defined 2D and 3D architectures.<sup>[18-22]</sup>

Despite the tremendous progress in preparation of the nano-size porphyrin- and phthalocyanine-based structures, such as wire- or tape-type assemblies, the preparation of well-defined 3D architectures similar to carbon-based nanotubes, fullerenes, or nanocages remains a big challenge to experimentalists. If one would like to enhance the optical properties and fluorescence quantum yields of individual phthalocyanine-based systems, it is necessary to design new 3D phthalocyanine-based nanostructures. In addition to new optical properties, these functional nanostructures can potentially be used in catalysis, molecular electronics, sensoric applications, and methane gas storage. The last potential application is of particular interest as the new technological challenges require materials for effective methane storage. Although some sporadic theoretical predictions on stability, optical properties, and hydrogen absorption in porphyrin and phthalocyanine nano-complexes were reported,<sup>[21,22]</sup> there is no systematic study on the electronic structures, topology, porosity, optical properties, and methane gas storage capacity of the prospective 3D porphyrin- or phthalocyanine-based nanocages or nanobarrels (simplest analogues of nanotubes) that has been reported so far. Thus, the aim of this study is to provide a general design for functional 3D tetraazaporphyrin-based nanostructures, which would bridge the gap between the well-known fullerenes and nanotubes and a new class of the functional-based nanomaterials. In order to achieve this goal, we explored three major motifs for functional nanostructures which vary by three- or four-fold topology, porosity, degree of

conjugation, and electronic structures (Figure 1). Since it is expected that all new nanostructures will have large pores, we also studied methane adsorption by these compounds as it allows probing a difference between transition-metal and main group element structural motifs.

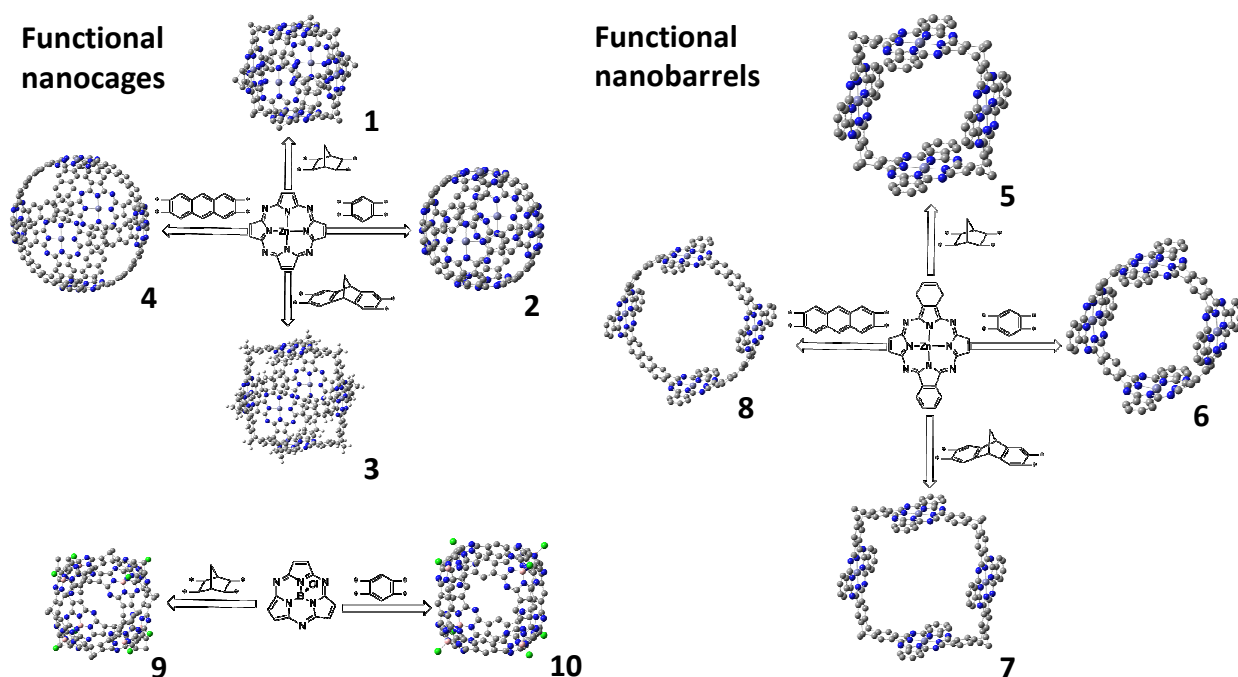


**Figure 1.** Proposed functional nanostructures 1 - 10.

### Computational details.

The geometry optimization and vibrational analyses of the proposed tetraazaporphyrin and subtetraaaporphyrin-based structures, totally 10 nanosystems, were performed at Becke's three-parameter hybrid exchange functional<sup>[23]</sup> coupled with the Lee-Yang-Parr nonlocal correlation functional<sup>[24]</sup> (B3LYP) level. In all cases the standard Wachter's full-electron and 6-31G(d) basis sets<sup>[25]</sup> were used for zinc and all other atoms, respectively. The redundant internal coordinate procedure was used during optimizations and the vibrational frequencies were calculated from the second derivative of the total energy with respect to atomic displacement about the

equilibrium geometry. These structures are indeed (at least local) minima as all DFT predicted frequencies were found to be positive. A time-dependent density functional theory (TDDFT) has been applied for calculations of excited states. We used the specially designed LC-wPBE exchange-correlation functional<sup>[26]</sup> and mentioned above large basis sets as in the case of frequency calculations. Depending on the nanostructure size, the number of the TDDFT-calculated excited states was varied between 120 and 180 to achieve convergence of states in a reasonable time (<90 days on 32 processors). All DFT and TDFT calculations were performed using the Gaussian 09 package.<sup>[27]</sup>

In order to estimate the methane uptake, the Grand Canonical Monte Carlo (GCMC) simulations<sup>[28,29]</sup> were applied within the LAMMPS code.<sup>[30]</sup> The Lennard-Jones (LJ) potential were used for methane

$$U_{CH_4-CH_4}(r) = 4\varepsilon_{CH_4} \left[ \left( \frac{\sigma_{CH_4}}{r} \right)^{12} - \left( \frac{\sigma_{CH_4}}{r} \right)^6 \right], \quad (1)$$

with parameters  $\sigma_{CH_4} = 3.73 \text{ \AA}$  and  $\varepsilon_{CH_4} = 1.2092 \text{ kJ/mol}$  for spherically symmetric particles.<sup>[31]</sup> For atoms of studied nanostructures the generic OPLS-AA force field parameters were selected.<sup>[32]</sup>

This force field is widely used for many types of organic compounds for classical MD simulations. Moreover, the OPLS-AA force field includes the parameters for zinc atoms and already applied for empirical calculations of supramolecules complexes with Zn-porphyrins in agreement with experimental data.<sup>[33]</sup> The methane isotherms for all compounds were measured in the pressure range of 1–10 MPa at 298 K and constant volume. For each given pressure  $2.5 \times 10^6$  Monte Carlo steps were used for both equilibration and following estimation of adsorption molecules. For each given pressure  $2.5 \times 10^6$  Monte Carlo steps were used for both equilibration and following estimation of adsorption molecules. Each Monte Carlo step consisted

of an attempted translation, insertion, deletion of a methane molecule. New configuration of the system for the translation case is accepted by using normal Metropolis method.<sup>[29]</sup> In the case of methane insertion, a new system configuration is accepted with the following probability:

$$p = \min\left(1, \frac{fV}{NkT} \exp\left[-\frac{\Delta U}{kT}\right]\right), \quad (2)$$

and for particle removal, the probability of the accepted configuration is:

$$p = \min\left(1, \frac{NkT}{fV} \exp\left[-\frac{\Delta U}{kT}\right]\right), \quad (3)$$

where  $V$  is the volume of the system,  $f$  is the fugacity of a guest molecules gas phase at the modeling condition (pressure, temperature),  $k$  is Boltzmann's constant,  $N$  is total number of particles,  $T$  is temperature, and  $\Delta U$  is energy difference of this two configuration.

First, the proposed method has been applied to calculate the methane adsorption isotherm in the case of gas clathrate hydrate and the results are shown in Figure S1. The methane content continues to increase due to the filling of methane in the hydrate cavities by increasing the pressure. From pressure of 4 MPa, the amount of methane is saturated and reached the maximum around  $170 \text{ cm}^3(\text{STP})/\text{cm}^3$  which is close to the Department of Energy (DOE) storage target.<sup>[34]</sup> This value is in agreement with the uptake value of  $180 \text{ cm}^3(\text{STP})/\text{cm}^3$  estimated in the ideal case if every hydrate cavity were filled with one methane molecule.<sup>[35]</sup> This verifies the validity of the simulation procedure. Moreover, the experimental value of uptake methane for methane gas hydrate obtained using dry water (a powder prepared by mixing water and silica particles) is found to be  $175 \text{ cm}^3(\text{STP})/\text{cm}^3$  at  $T= 273 \text{ K}$  and  $2.73 \text{ MPa}$ .<sup>[36]</sup>

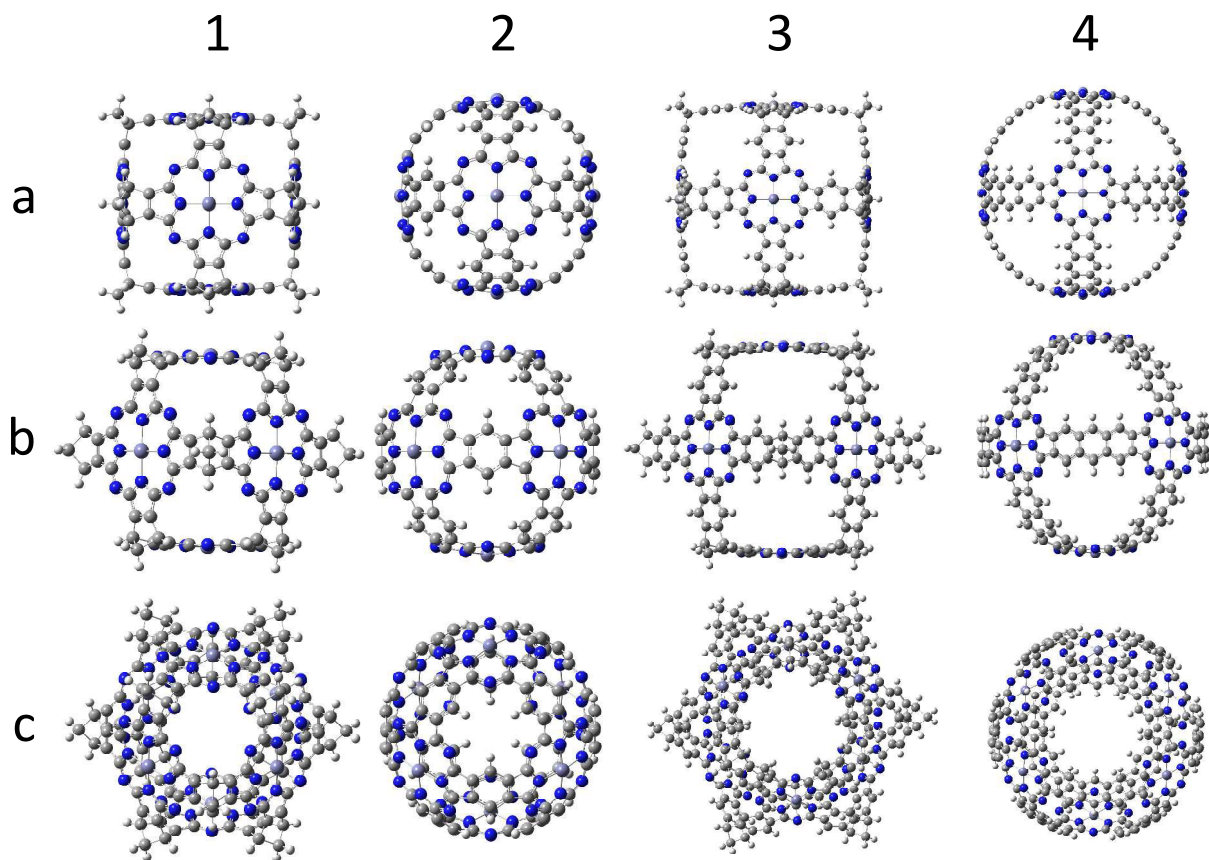
In order to estimate gas adsorption, we arranged our structures in a molecular crystal form. The cubic cell for the single molecules was selected and the lattice parameters were calculated using the periodic density functional calculations within the Vienna *ab initio* Simulation Package

(VASP)<sup>[37]</sup>. The generalized gradient approximation (GGA) with Perdew, Burke, and Ernzerhof (PBE) parametrization<sup>[38]</sup> and all-electron projector augmented wave (PAW) method<sup>[39]</sup> was used for the estimation of the electron exchange-correlation and the interaction between ion cores and valence electrons, respectively. The plain-wave cutoff energy was 400 eV and convergence in energy ( $10^{-4}$  eV) and force ( $3 \times 10^{-3}$  eV/Å) were used during the optimization procedure. Brillouin zone integrations were performed using the Monkhorst-Pack k-point mesh<sup>[40]</sup> with a  $3 \times 3 \times 3$  grid. The calculations were carried out using the van der Waals (vdW) corrected exchange correlated DFT potential within the Grimme method<sup>[41]</sup>. Additionally, the ab initio molecular dynamics (MD) simulations have been performed within VASP code in order to investigate the stability of proposed structures. All simulations are carried out at 300 K for 5000 steps with a time step of 0.2 fs in a canonical (NVT) ensemble using the algorithm of Nosé-Hoover thermostat.<sup>[42]</sup>

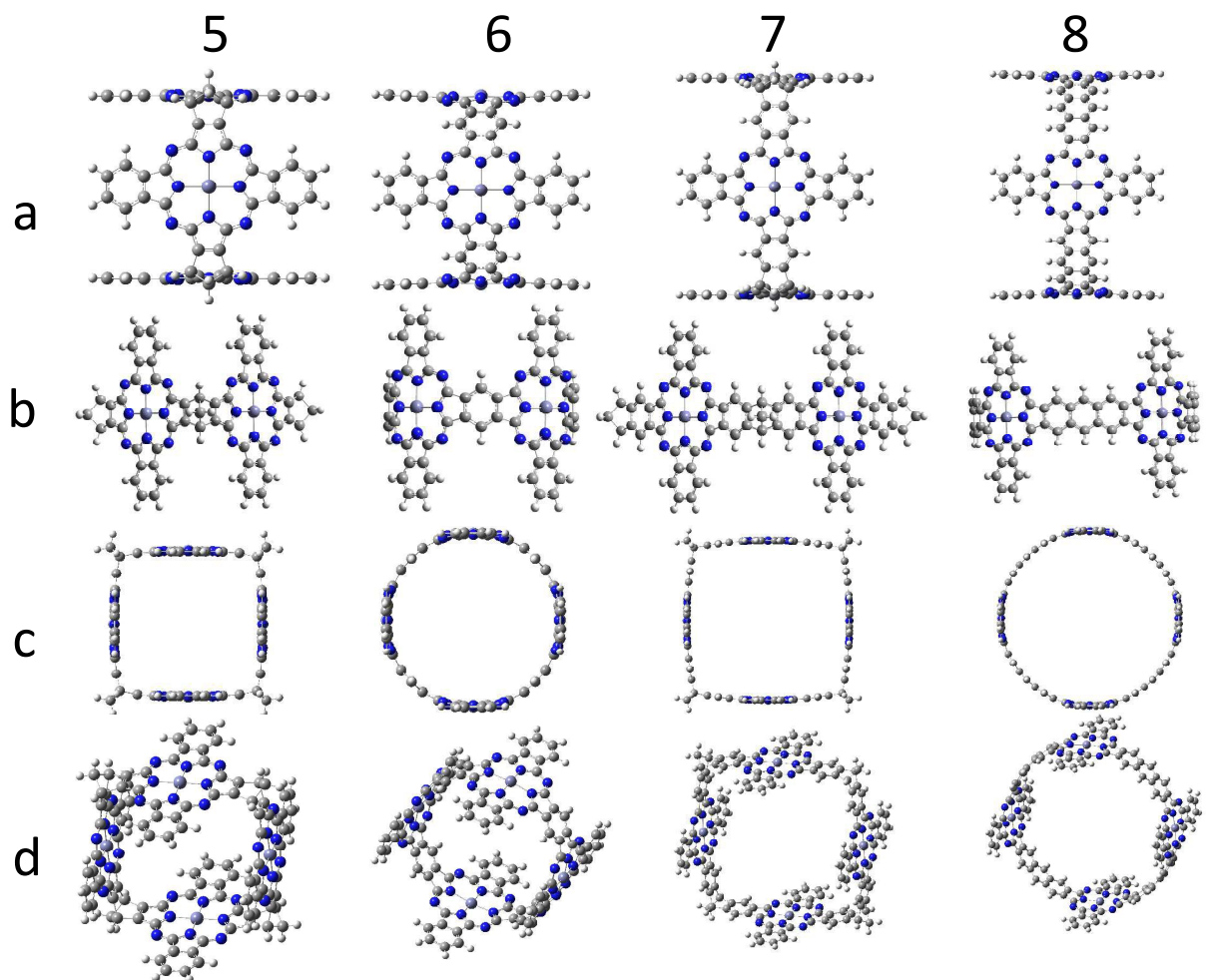
## **Results**

***Design of tetraazaporphyrin-based nanocages and nanobarrels.*** Our basic design of the functional nanostructures was pointed toward three general motifs. The first nanocage motif is presented in nanocages **1** - **4** (Figure 1). In this motif, six individual tetraazaporphyrin-type fragments are combined to form four different nanocages. In two of them, nanocages **1** and **3**, the conjugation between the tetraazaporphyrin-type fragments has been interrupted by the bridging  $sp^3$  carbon groups. In the other two, nanocages **2** and **4**, all individual carbon fragments are completely conjugated with each other by bridging benzene groups consisting of  $sp^2$  carbon atoms. The conjugation bridge of nanocage **2** consists of a single benzene ring, while in case of the larger nanocage **4**, the individual tetraazaporphyrin fragments are bridged by anthracene groups. All four nanocages **1** - **4** have octahedral symmetry, four-fold local symmetry of the individual tetraazaporphyrin fragments, and were optimized in the  $O_h$  point group. In the second

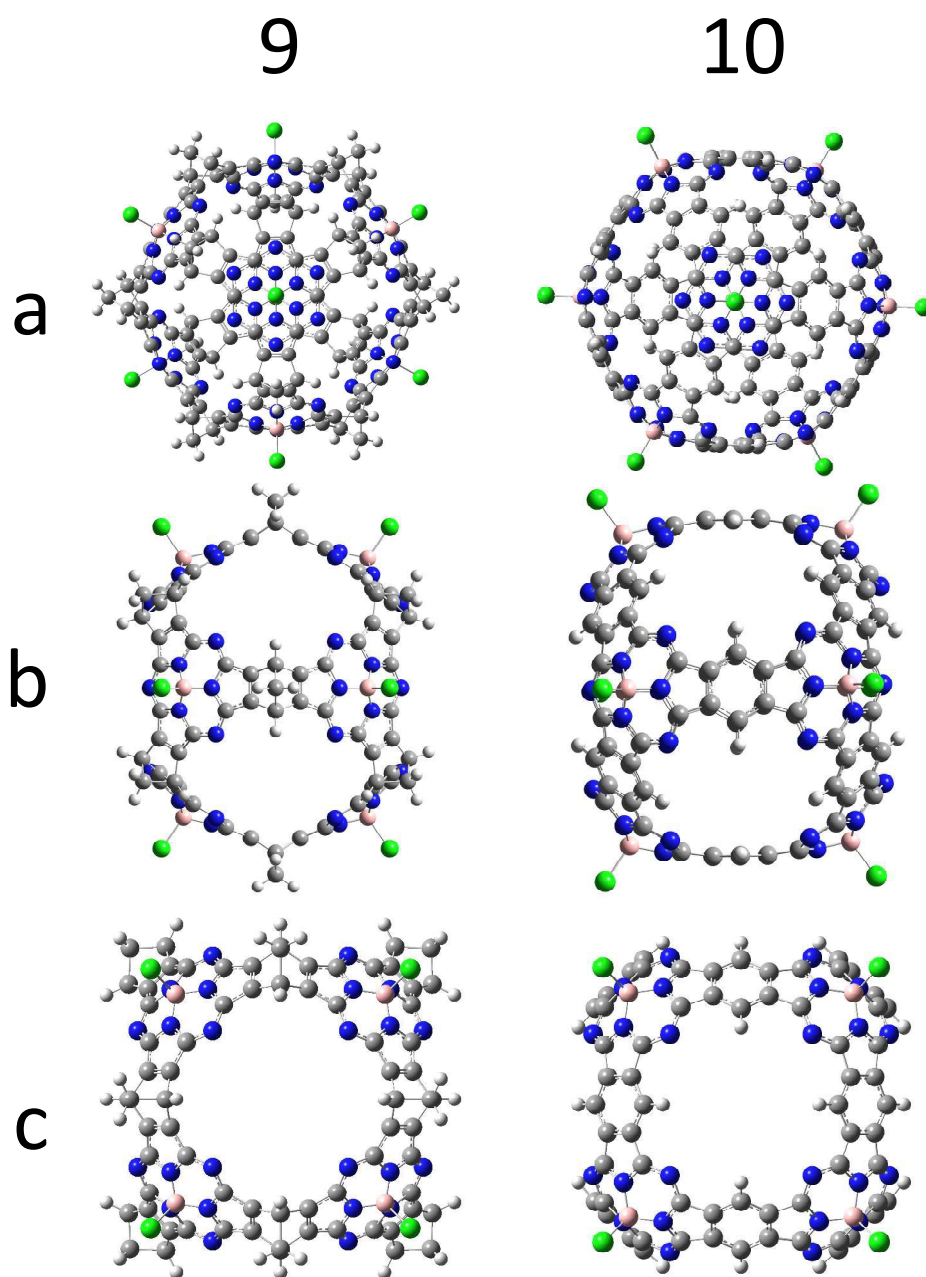
motif, nanobarrels **5** - **8** (Figure 1), four individual tetraazaporphyrin fragments were connected by aromatic (nanobarrels **6** and **8**) or non-aromatic (nanobarrels **5** and **7**) bridging groups. Again, the conjugation in nanobarrel **6** is provided by a single benzene ring, while an anthracene bridge facilitates the conjugation in nanobarrel **8**. All of the functional nanobarrels **5** - **8** have four-fold total symmetry, two-fold local symmetry of the individual tetraazaporphyrins, and were optimized in the  $D_{4h}$  point group. In the last design motif, we used a three-fold subtetraazaporphyrin platform to form functional nanocages **9** and **10** (Figure 1). In this case, because of the three-fold symmetry of the subtetraazaporphyrin precursor, the minimum number of subtetraazaporphyrin fragments in the individual nanocages should be eight. Again, nanocage **9** was designed such that the bridging  $sp^3$  carbons would interrupt conjugation between the individual subtetraazaporphyrin fragments. In the case of nanocage **10**, however, aromatic benzene rings should facilitate conjugation between the individual subtetraazaporphyrin units. The last motif has an octahedral geometry, eight three-fold individual subtetraazaporphyrin units and was optimized in the  $O_h$  point groups.



**Figure 2.** Perspective views (a - c) of the DFT-optimized structures functional nanocages **1 - 4**.



**Figure 3.** Perspective views (a - d) of the DFT-optimized structures functional nanobarrels 5 - 8.

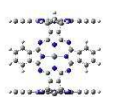
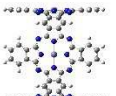
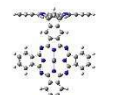
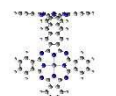
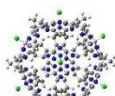
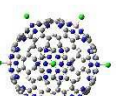


**Figure 4.** Perspective views (a - c) of the DFT-optimized structures functional nanocages **9 - 10**.

***DFT predicted geometries and stabilities.*** The DFT-predicted geometries of the functional 3D nanostructures **1 - 10** are shown in Figures 2 - 4. All calculated nanocages and nanobarrels were

found to be considerably larger than the size of the standard C<sub>60</sub> fullerene and varies with the type and size of the bridging fragments. In general, the diameters of all systems were found to be in the 1.2 to 2.5 nm range. Because of the close-to-spherical geometry of nanocages **2**, **4**, and **10**, it is easier to compare their sizes (Table 1). Indeed, nanocage sizes for the largest carbon-carbon contacts vary between 1.39 (nanocage **2**) to 2.01 (nanocage **4**) nm. Similarly, the longest Zn-Zn or Cl-Cl distances in nanocages **2**, **4**, and **10** vary between 1.35 and 2.02 nm. Similar trend was observed also for non-conjugated nanocages **1**, **3**, and **9** where the Zn-Zn and Cl-Cl distances vary between 1.22 and 1.98 nm. Similar Zn-Zn distances can be used to estimate the size of the pore in functional nanobarrels **5** - **8**. Estimated pore size varies between 1.21 and 1.98 nm for nanotube **5** and **8**, respectively. It is interesting to point out that the nanocages **1** - **4** and **9** - **10** have also large pores accessible for small molecules. For instance, in the case of cage **4**, the H<sub>9A</sub> to H<sub>10B</sub> (H<sub>9A</sub> represents the hydrogen at 9<sup>th</sup> position of the anthracene bridge and H<sub>10B</sub> represents the hydrogen at the 10<sup>th</sup> position of the neighboring anthracene bridge) bond distance in the three-fold symmetry pore is 6.55 Å, which translates into a pore diameter of 3.78 Å. Similarly, the three-fold pore in nanocage **2** was estimated to have a 1.98 Å diameter. Finally, in the case of the subtetraazaporphyrin cage **10** the diameter of the four-fold symmetry pore was estimated to be 4.71 Å. The stability of all proposed nanostructures **1** - **10** was confirmed by frequency calculations which show no imaginary frequencies in optimized structures. In order to investigate the dynamic stability of the proposed structures, we performed *ab initio* molecular dynamics (MD) simulations. During the simulations, the symmetry constraint was omitted. After 1000 fs, all structures remained intact although some rather minor deformations can be clearly seen (Figures S2-S5). Thus, our MD simulations are indicative that all of the nanocages and nanobarrels presented above are dynamically stable.

**Table 1.** Selected distances in DFT-optimized nanostructures **1 - 10**.

Structure	Distance (nm)	Structure	Distance (nm)
<b>Nanocage 1</b>		<b>Nanobarrel 5</b>	
	Zn-Zn 1.216		Zn-Zn 1.207
	C-C 1.592		C-C 1.589
	C-C 1.787		C-C 1.784
<b>Nanocage 2</b>		<b>Nanobarrel 6</b>	
	Zn-Zn 1.352		Zn-Zn 1.350
	C-C 1.391		C-C 1.367
<b>Nanocage 3</b>		<b>Nanobarrel 7</b>	
	Zn-Zn 1.741		Zn-Zn 1.740
	C-C 2.258		C-C 2.258
	C-C 2.458		C-C 2.458
<b>Nanocage 4</b>		<b>Nanobarrel 8</b>	
	Zn-Zn 1.968		Zn-Zn 1.979
	C-C 2.015		C-C 1.991
<b>Nanocage 9</b>		<b>Nanocage 10</b>	
	B-B 1.598		B-B 1.650
	Cl-Cl 1.980		Cl-Cl 2.024
	C-C 1.874		C-C 1.482

We also calculated the Gibbs energy for a hypothetical formation reaction of the nanostructures **1 - 10**. The proposed reaction profiles are shown in Schemes S1-S5. It has been found that all formation reactions of the nanostructures are endothermic and the formation of the nanobarrels are less endothermic than that of the nanocages. Our thermochemical predictions are quite

expected as they reflect the degree of steric strain during the formation of the curved nanostructures **1** - **10**.

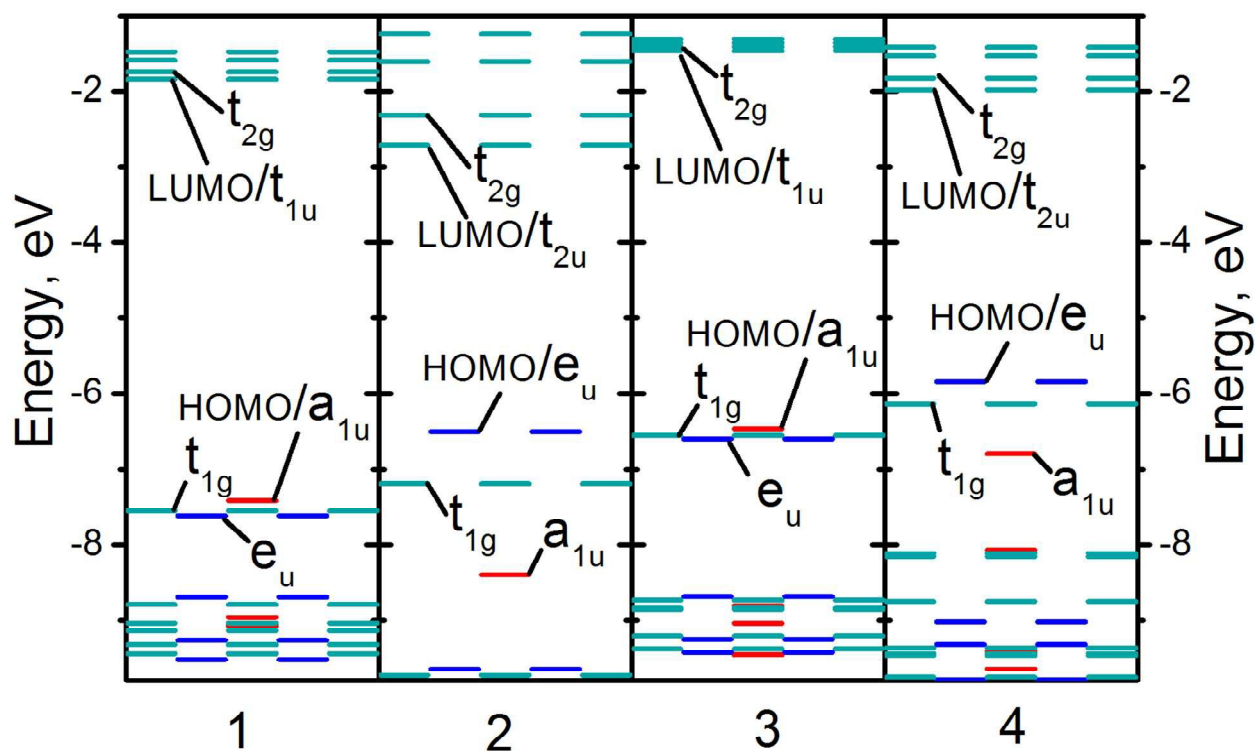


**Figure 5.** DFT-predicted molecular orbital diagram for nanocages **1** - **4**. Non-degenerate MOs are in red, doubly degenerate MOs are in blue, and triply degenerate MOs are in grey.

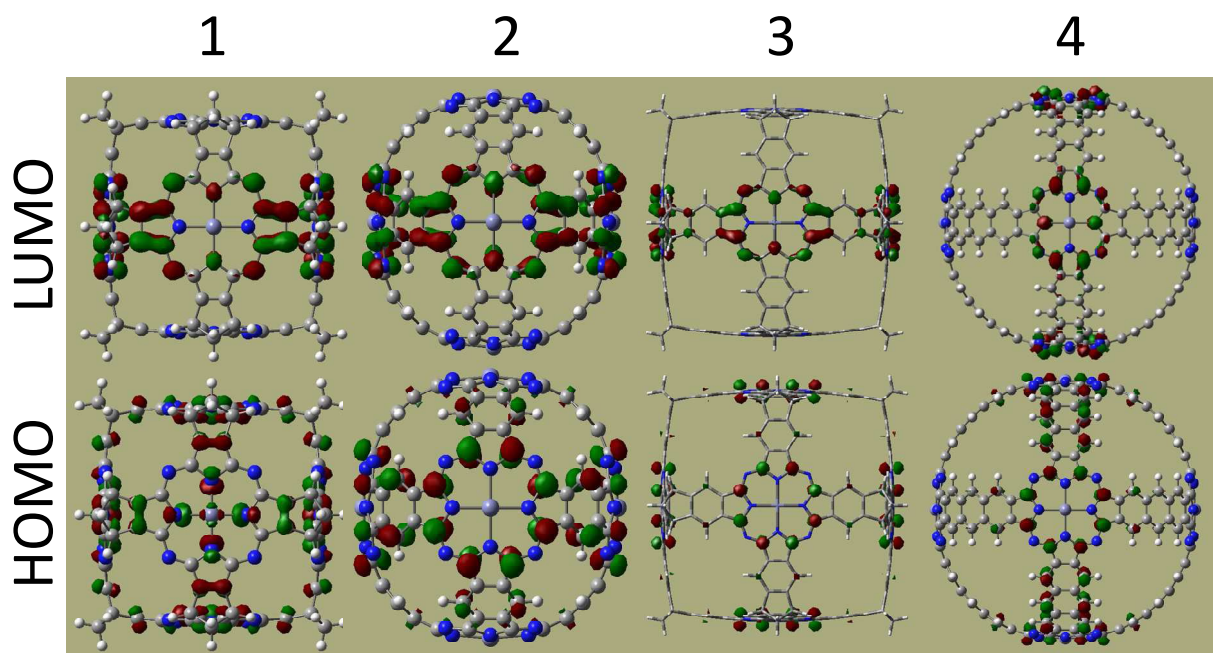
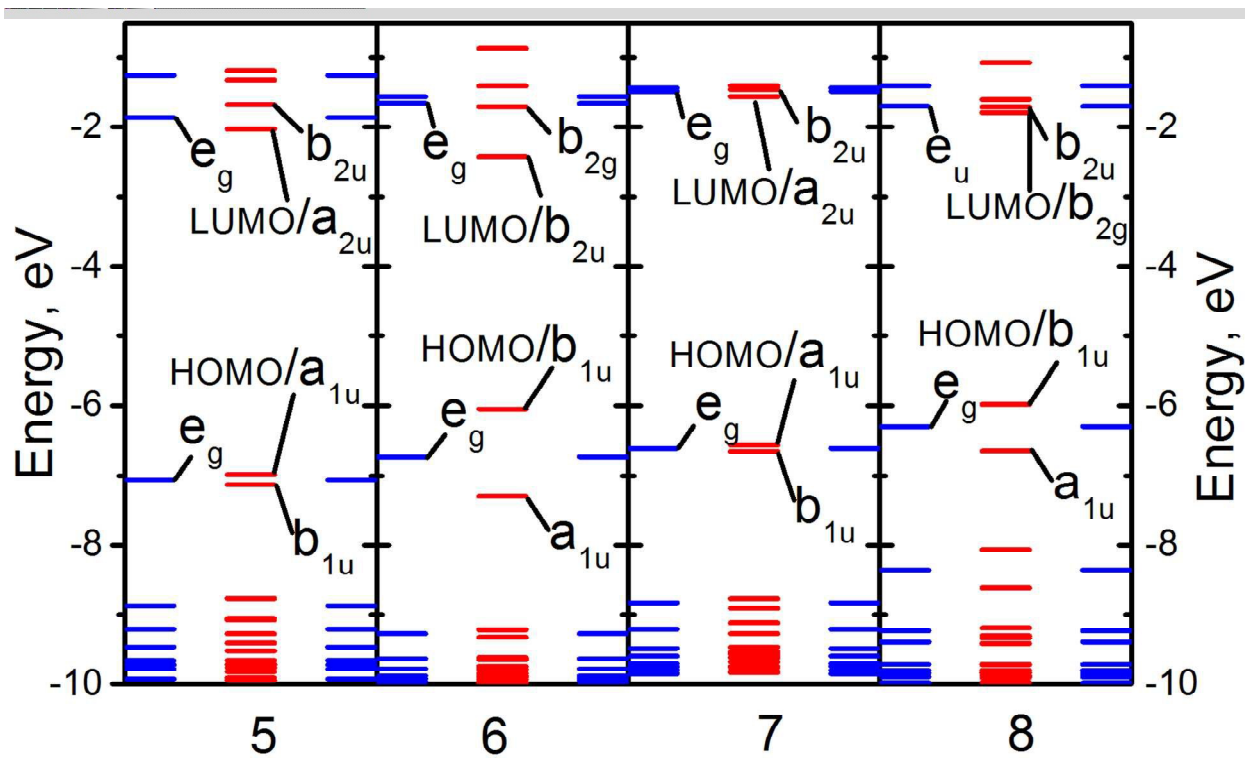
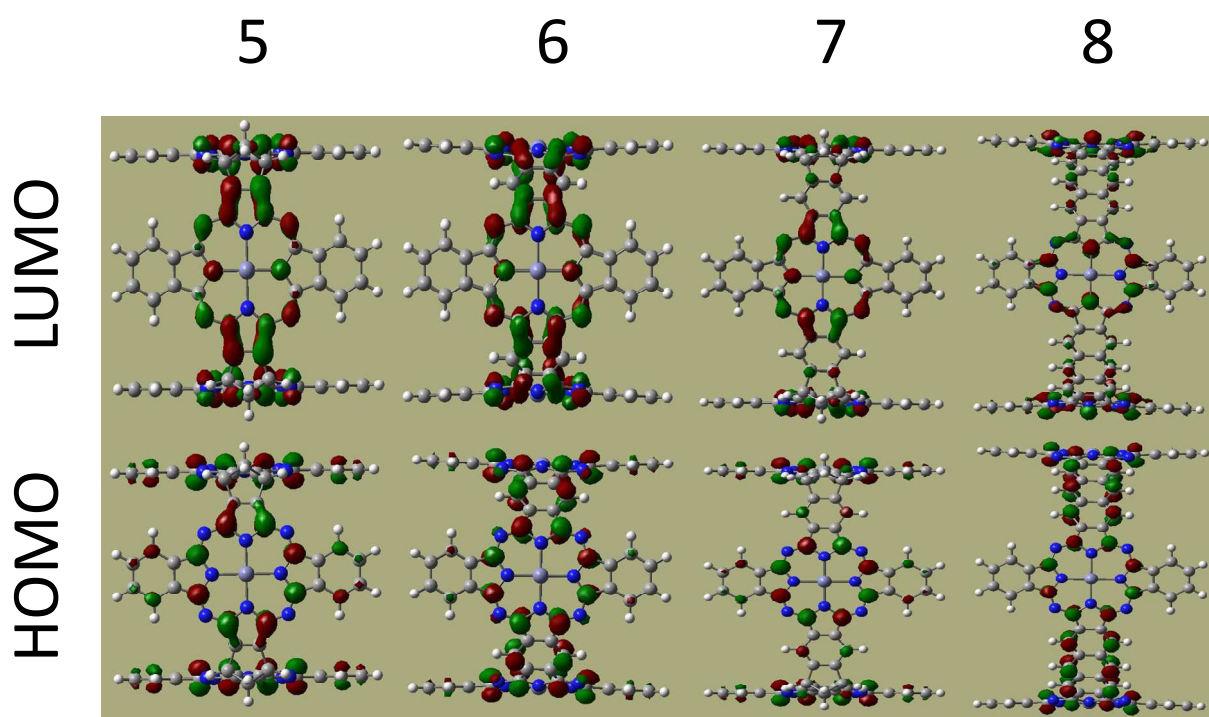


Figure 6. DFT-predicted frontier molecular orbitals for nanocages 1 - 4.



**Figure 7.** DFT-predicted molecular orbital diagram for nanobarrels **5 - 8**. Non-degenerate MOs are in red and doubly degenerate MOs are in blue.



**Figure 8.** DFT-predicted frontier molecular orbitals for nanobarrels **5 - 8**.

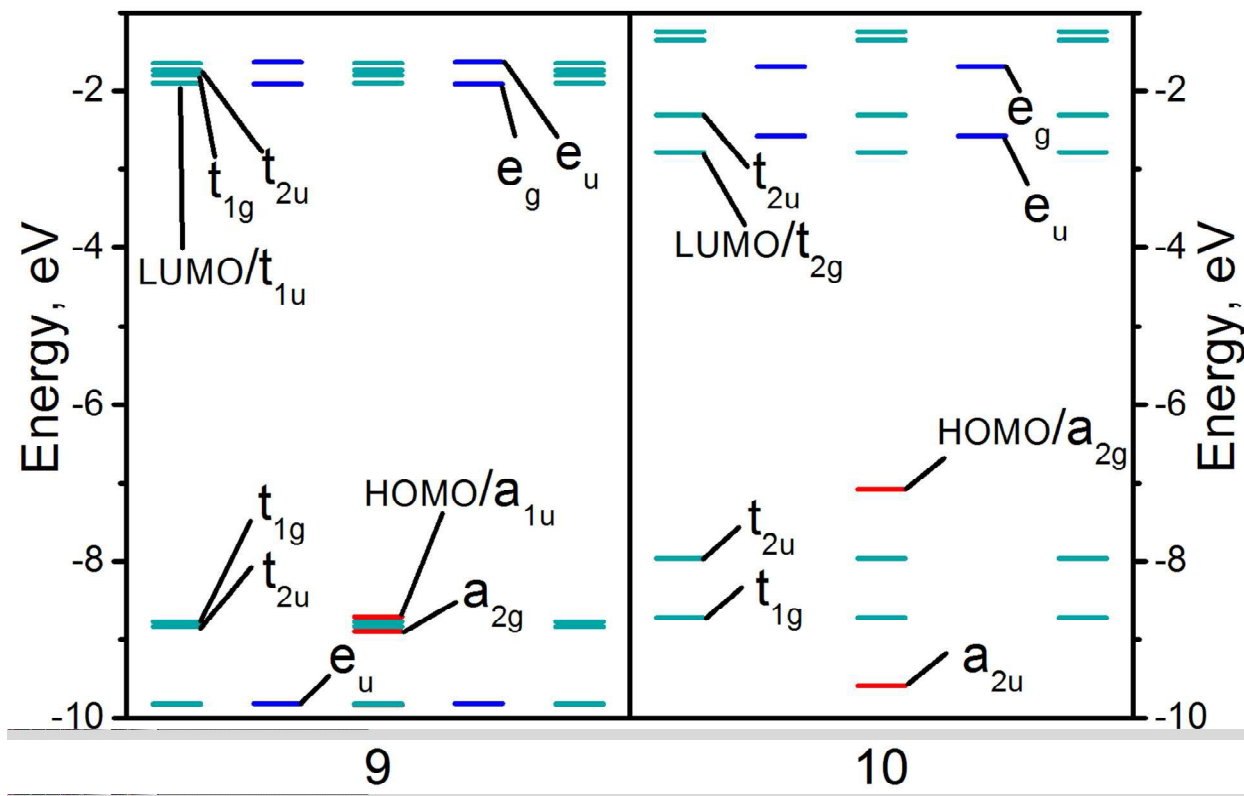


**Figure 9.** DFT-predicted molecular orbital diagram for nanocages **9** and **10**. Non-degenerate MOs are in red, doubly degenerate MOs are in blue, and triply degenerate MOs are in grey.

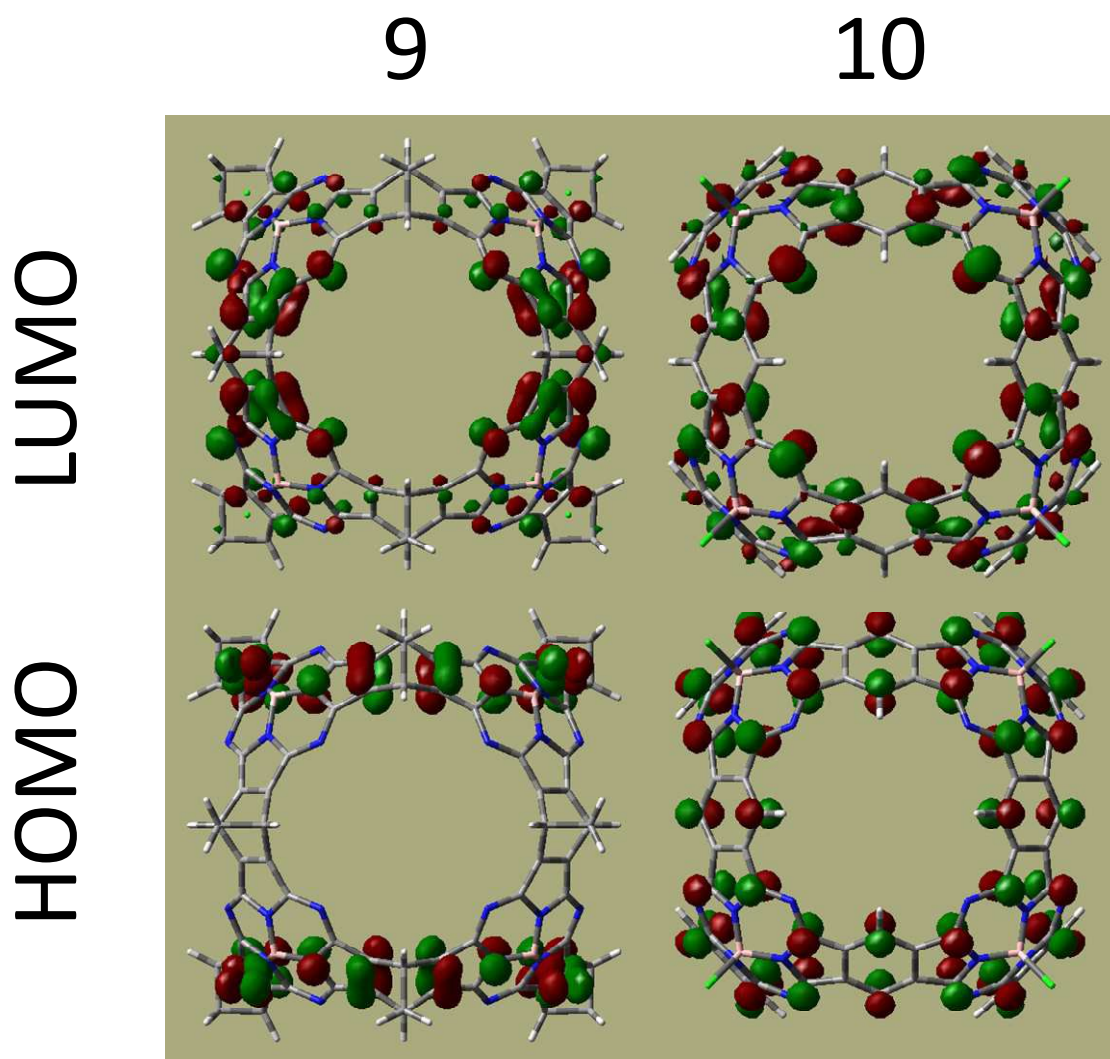


**Figure 10.** DFT-predicted frontier molecular orbitals for nanocages **9** and **10**.

*Electronic structures.* The DFT predicted energy diagrams for nanocages **1** - **4** are presented in Figure 5 and Supporting Information Figure S6, while the frontier orbitals for the same cages are shown in Figure 6 and Supporting Information Figures S7 – S10. From the DFT calculations, several trends are clear for the electronic structures of these nanocages. First, the HOMO orbitals in the non-conjugated nanocages **1** and **3** have lower energies than the HOMO orbitals in the

corresponding conjugated nanocages **2** and **4**, which is indicative of their lower oxidation potential compared to **1** and **3**, respectively. Similarly, the energies of the LUMOs in the non-conjugated nanocages **1** and **3** are considerably higher than the LUMOs of the conjugated nanocages **2** and **4** making the HOMO - LUMO gap for the non-conjugated nanocages (5.58 eV for **1** and 5.00 eV for **3**) significantly larger than the conjugated nanocages (3.79 eV for **2** and 3.86 eV for **4**). The HOMO in the non-conjugated cages **1** and **3** has  $a_{1u}$  symmetry while the HOMO for conjugated nanocages **2** and **4** has doubly degenerate  $e_u$  symmetry. It is interesting to note that the HOMO in nanocage **1** has a significant contribution from the isoindole nitrogen atoms while in all other cases the HOMO has no contribution from the nitrogen atoms. The next observation is that the bridging fragments provide significant contribution into the HOMO in the conjugated structures **2** and **4** while no similar contribution was observed in the case of non-conjugated systems **1** and **3**. The HOMO in a smaller nanocage **1** is 0.91 eV more stable than the same orbital in nanocage **3** while similar difference is seen in HOMO energies in conjugated nanocages in **2** and **4** (0.63 eV). The LUMO orbitals in the case of non-conjugated nanocages **1** and **3** are of  $t_{1u}$  symmetry, while the LUMO orbitals for the conjugated nanocages **2** and **4** have  $t_{2u}$  symmetry. In general, the first three sets of the occupied MOs ( $a_{1u}$ ,  $e_u$ , and  $t_{1g}$  symmetry) in non-conjugated systems **1** and **3** were found in close energy proximities ( $\Delta E$  is 0.20 eV for **1** and 0.13 eV for **3**) while no such accidental degeneracy has been seen for the same set of the orbitals in the case of the conjugated nanocages **2** and **4** ( $\Delta E$  is 1.89 eV for **1** and 0.96 eV for **4**). Similarly, the first four sets of triply degenerate unoccupied orbitals ( $t_{1u}$ ,  $t_{2u}$ ,  $t_{1g}$ , and  $t_{2g}$  symmetries) in the case of non-conjugated cages **1** and **3** are very closely spaced in energy ( $\Delta E$  is 0.36 eV for **1** and 0.16 eV for **3**) while similar orbitals in the case of the conjugated cages **2** and **4** are much better separated in energies ( $\Delta E$  is 1.48 eV for **1** and 0.55 eV for **3**).

In the case of the nanobarrels **5** - **8**, the HOMO and the LUMO orbitals both were found to be non-degenerate molecular orbitals, which reflects the change in symmetry from octahedral  $O_h$  to tetragonal  $D_{4h}$ . The general trends in the electronic structures of nanobarrels **5** - **8**, however, resemble those observed earlier for nanocages **1** - **4** (Figures 7 and 8 as well as Supporting Information Figures S11 - S15). In particular, the HOMOs in all nanotubes have major contributions from the  $\alpha$ -pyrrolic carbons of tetraazaporphyrin rings. Next, no contributions from saturated  $sp^3$  carbon-based linking fragments were found in the HOMO region for the nanobarrel **5** and **7** while significant contribution from the aromatic regions was found in the HOMO orbitals in conjugated nanobarrel **6** and **8**. The HOMO - LUMO energy gap in the non-conjugated nanobarrel **5** and **7** (4.96 eV for **5** and 5.00 eV for **7**) were found to be significantly larger than in the corresponding conjugated nanobarrels **6** and **8** (3.63 eV for **6** and 4.20 eV for **8**). The HOMO in non-conjugated nanotubes **5** and **7** are significantly more stable than the HOMO in conjugated systems **6** and **8** (0.94 eV difference for **5** - **6** pair and 0.58 eV difference for **7** - **8** pair), which is indicative of lower oxidation potentials in **6** and **8** compared to **5** and **7**, respectively. Finally, the four highest occupied molecular orbitals ( $a_{1u}$ ,  $b_{1u}$ , and  $e_g$  symmetries) of the non-conjugated nanobarrels **5** and **7** are more closely spaced in energy ( $\Delta E$  is 0.15 eV for **5** and 0.09 eV for **7**) than the same orbitals in the conjugated nanobarrels **6** and **8** ( $\Delta E$  is 1.25 eV for **6** and 0.66 eV for **8**). The HOMO symmetries in non-conjugated systems **5** and **7** are all  $a_{1u}$  while those in the conjugated **6** and **8** are  $b_{1u}$ . The LUMO in all nanotubes have significant contribution from the nitrogen atoms and has  $a_{2u}$  (**5** and **7**) or  $b_{2u}$  (**6** and **8**) symmetry.

The electronic structure of the subtetraazaporphyrin nanocages **9** and **10** are shown in Figures 9 and 10 and Supporting Information Figures S16 - S18. Again, these correlate well with the trends found for nanocages **1** - **4**. Indeed, the HOMO - LUMO energy gap in non-conjugated nanocage

**9** (6.79 eV) is much larger than the HOMO - LUMO energy gap in conjugated nanocage **10** (4.30 eV). These HOMO - LUMO energy gaps are the largest for non-conjugated and conjugated nanocages and nanobarrels discussed in this paper. The HOMO in both nanocages **9** ( $a_{1u}$  symmetry) and **10** ( $a_{2g}$  symmetry) are non-degenerate and the energy is significantly lower (1.63 eV) in **9** compared to **10**, which is indicative of the lower oxidation potential of **10**. The LUMO in nanocage **9** is doubly degenerate ( $e_g$  symmetry) and the LUMO in nanocage **10** is triply degenerate ( $t_{2g}$  symmetry). Again, the contribution of the aromatic bridge in the conjugated nanocage **10** was found to be significant while no contribution from the bridging  $sp^3$  carbon atoms in nanocage **9** was observed in the HOMO region.

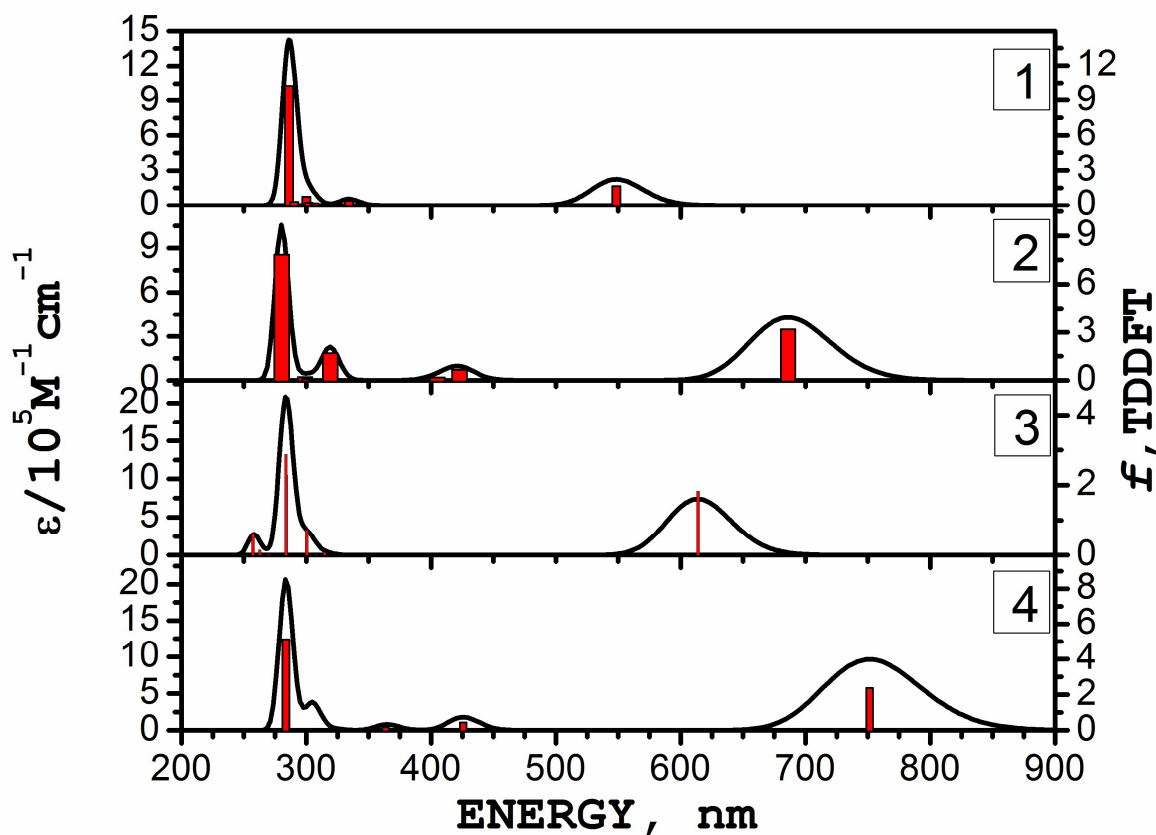


**Figure 11.** TDDFT-predicted UV-vis spectra for nanocages **1** - **4**.

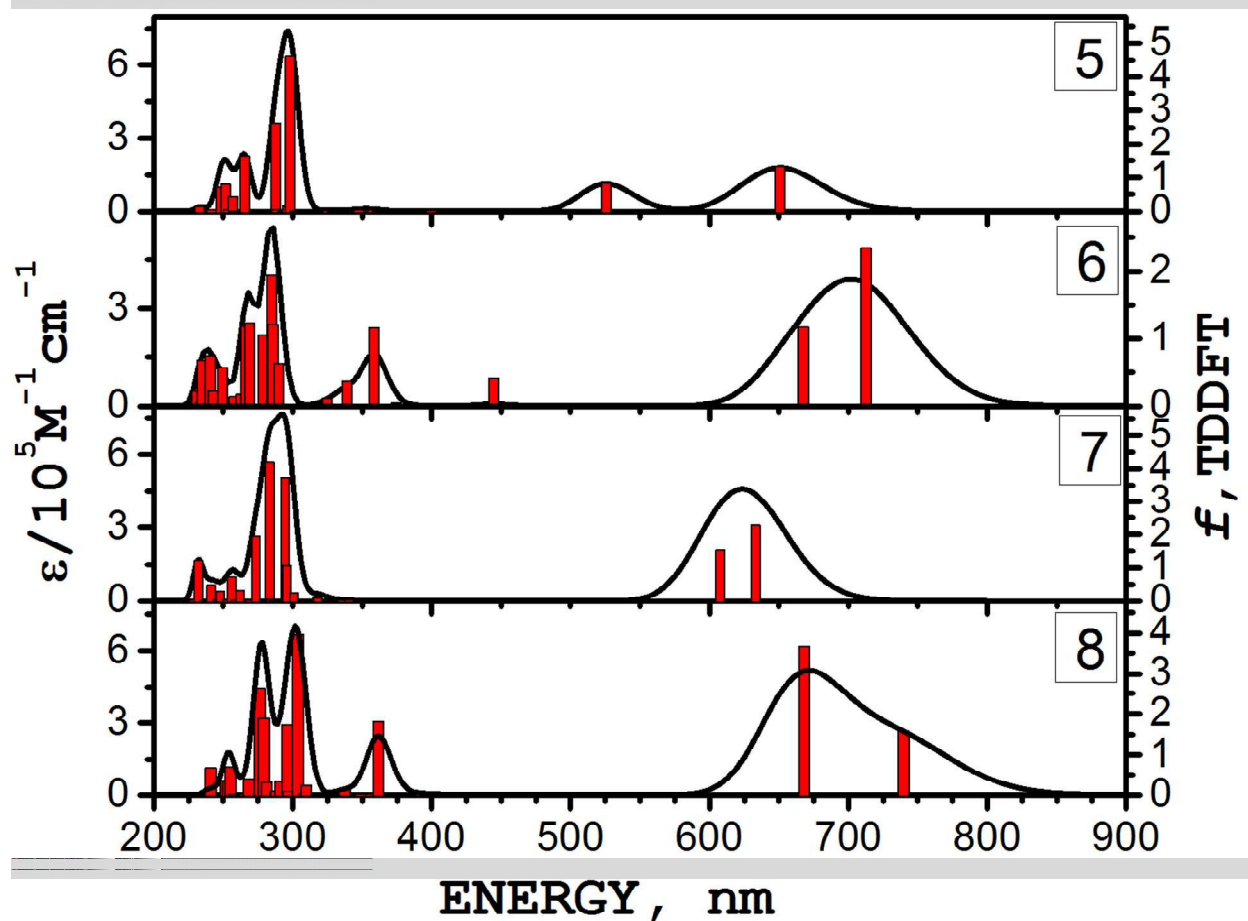
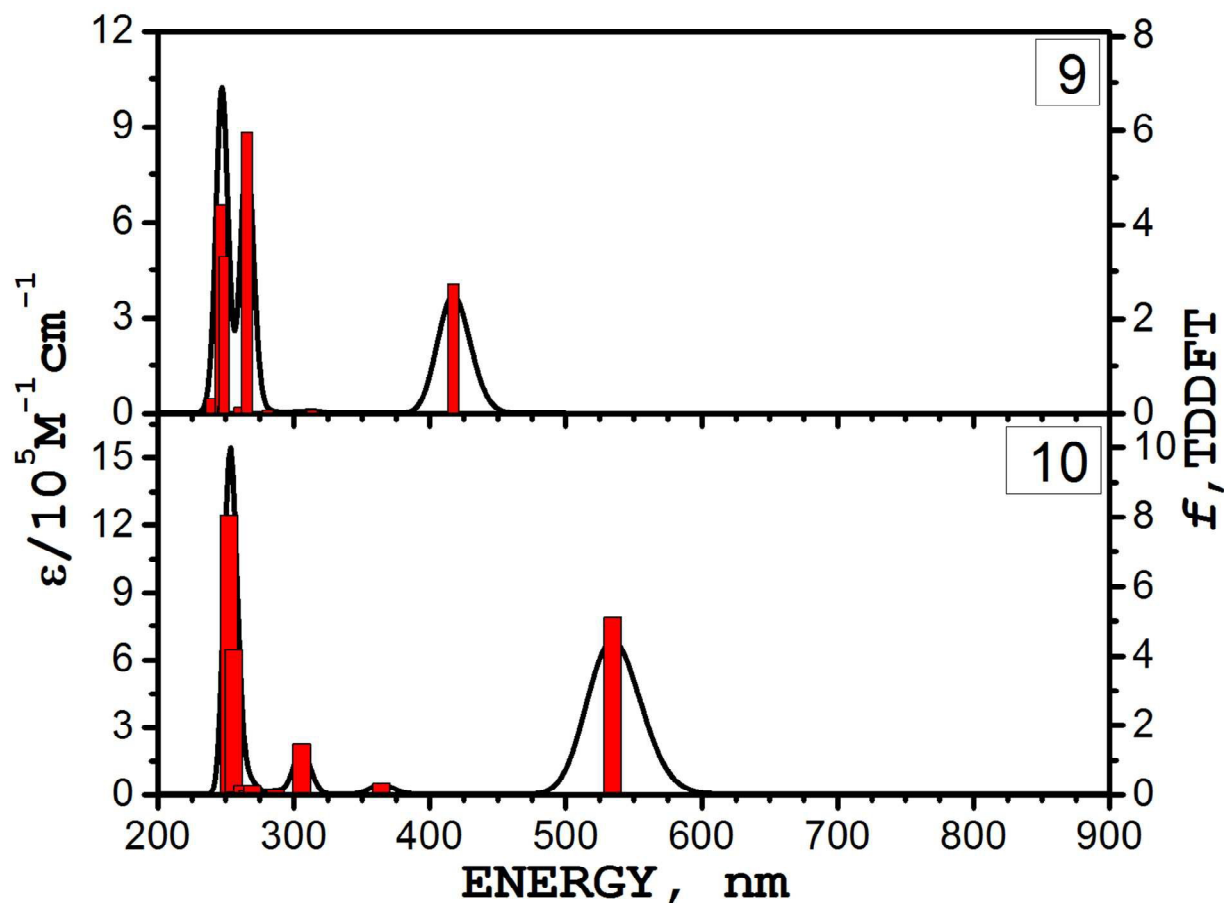


Figure 12. TDDFT-predicted UV-vis spectra for nanobarrels 5 - 8.



**Figure 13.** TDDFT-predicted UV-vis spectra for nanocages **9** and **10**.

*UV-vis spectra of nanostructures 1 - 10.* Similar to the CdSe clusters and extended porphyrin assemblies, one might expect that the standard exchange-correlation functions, such as B3LYP, would not be able to predict accurately intramolecular charge transfer energies for  $\pi$ - $\pi^*$  transitions in nanosystems **1** - **10** because of their potential long-range character.<sup>[43]</sup> Thus, in order to overcome these potential obstacles, we used the specifically designed long-range corrected exchange-correlation functional LC-wPBE,<sup>[26]</sup> which was shown to improve the TDDFT predicted vertical excitation energies in the supramolecular systems.<sup>[44]</sup> The choice of

the LC-wPBE exchange-correlation functional instead of the more common CAM-B3LYP exchange-correlation functional for TDDFT calculations was dictated by the well-documented trend of CAM-B3LYP to overestimate by  $\sim 0.3\text{-}0.5\text{eV}$  vertical excitation energies of the  $\pi\text{-}\pi^*$  transitions in porphyrins and their analogues.<sup>[45]</sup>

The TDDFT predicted UV-vis spectra for nanostructures **1** - **10** are shown in Figures 11 - 13. In addition, we have calculated three calibration spectra of zinc tetraazaporphyrin (ZnTAP), zinc phthalocyanine (ZnPc) and zinc antraphthalocyanine (ZnAcN) using the same TDDFT approach (Supporting Information Figure S19). In the case of our calibration spectra, the calculated *Q*-band transitions in monomeric ZnTAP, ZnPc, and ZnAcN complexes at 546, 623, and 746 nm, respectively, correlate well with the corresponding experimental data on the same systems and dominated by the classic HOMO ( $a_{1u}$ )  $\rightarrow$  LUMO, LUMO+1 ( $e_g$ ) single-electron transitions giving a rise to  $^1E_u$  excited state. Similarly, the TDDFT predicted increase in oscillator strengths for ZnTAP ( $f = 0.15$ ), ZnPc ( $f = 0.46$ ), ZnAcN ( $f = 0.94$ ) correlate well with the experimental observed increase in experimental extinction coefficients of the *Q*-band for these compounds.<sup>[12m,17a]</sup> Again, our test calculations on ZnTAP, ZnPc, and ZnAcN using the CAM-B3LYP exchange-correlation functional indicates that this method tends to overestimate the energies of  $\pi\text{-}\pi^*$  transitions. It might be expected that the nanocages **1** and **3**, in which the saturated  $\text{sp}^3$  carbon bridges interrupt conjugation between the individual tetraazaporphyrin cores, would resemble the UV-vis spectra of parent ZnTAP and ZnPc, respectively. In agreement with this hypothesis, the lowest energy, symmetry-allowed transitions in nanocages **1** and **3** were predicted by TDDFT at 549 and 614 nm, respectively (Figure 11). Both of these symmetry-allowed  $^1T_u$  excited states are triply degenerate. DFT-predicted electronic structure of **1** and **3** indicative of the accidental degeneracy of the first 6 high-energy occupied and 12 low-

energy unoccupied MOs. Because of this situation, the  ${}^1T_{1u}$  excited state consists of the complex combination of the single-electron excitations (Supporting Information Table S1) and is dominated by the HOMO ( $a_{1u}$ )  $\rightarrow$  LUMO+6-LUMO+8 ( $t_{1g}$ ), HOMO-4-HOMO-5 ( $e_u$ )  $\rightarrow$  LUMO+3-LUMO+5 ( $t_{2g}$ ), and HOMO-1-HOMO-3 ( $t_{1g}$ )  $\rightarrow$  LUMO-LUMO+2 ( $t_{1u}$ ) transitions. In the case of fully conjugated nanocages **2** and **4** one might expect the low-energy shift of the  $Q$ -band like transitions. Not surprisingly, the symmetry-allowed triply degenerate low-energy excited states of the  ${}^1T_{1u}$  symmetry in nanocages **2** and **4** were TDDFT predicted to be red-shifted by  $\sim 140$  nm compared to non-conjugated nanocages **1** and **3**. A better separation in energy between the high-energy occupied MOs and significant stabilization of the  $a_{1u}$  orbital in nanocages **2** and **4** results in a situation when the major contribution into the lowest-energy excited states comes from the HOMO-HOMO-1 ( $e_u$ )  $\rightarrow$  LUMO+3-LUMO+5 ( $t_{2g}$ ) single-electron excitations complimented by the HOMO-2-HOMO-5 ( $t_{1g}$ )  $\rightarrow$  LUMO-LUMO+2 ( $t_{2u}$ ) transitions (Supporting Information Table S1). In addition, the conjugation in nanocages **2** and **4** also leads to significant increase of the oscillator strengths of the low-energy transitions compared to those in non-conjugated systems **1** and **3**. In the case of nanobarrels **5** - **8** the local symmetry of the macrocyclic chromophores decreased from the four-fold to two-fold and thus one might expect that the  $Q$ -band like transitions in the NIR region of the spectrum will be split into two bands similar to  $Q_x$  and  $Q_y$  bands observed in the case of metal-free tetraazaporphyrin. In agreement with this hypothesis, TDDFT-predicted spectra of nanobarrels **5** - **8** have two distinct transitions in the NIR region (Figure 12). One of these two being doubly degenerate  ${}^1E_u$  excited state and the other one being non-degenerate  ${}^1A_{2u}$  excited state, reflecting an overall decrease in symmetry from  $O_h$  symmetry in nanocages **1** - **4** to  $D_{4h}$  symmetry in nanobarrels **5** - **8**. In the case of non-conjugated nanobarrels **5** and **7**, the lowest energy  ${}^1E_u$  excited state predicted at 651 nm for **5** and

633 nm for **7** consists of nearly equal contributions from the HOMO ( $a_{1u}$ )  $\rightarrow$  LUMO+1-LUMO+2 ( $e_g$ ), HOMO-1-HOMO-2 ( $e_g$ )  $\rightarrow$  LUMO ( $a_{2u}$ ), HOMO-1-HOMO-2 ( $e_g$ )  $\rightarrow$  LUMO+3 ( $b_{2u}$ , **5**) or LUMO+7 ( $b_{2u}$ , **7**), and HOMO-3 ( $b_{1u}$ )  $\rightarrow$  LUMO+1-LUMO+2 ( $e_g$ ) single-electron excitations. The lowest energy  $^1A_{2u}$  excited state in nanobarrels **5** (525 nm) and **7** (608 nm) consists of almost equivalent contributions from the HOMO ( $a_{1u}$ )  $\rightarrow$  LUMO+7 ( $a_{2g}$ , **5**) or LUMO+6 ( $a_{2g}$ , **7**), HOMO-1-HOMO-2 ( $e_g$ )  $\rightarrow$  LUMO+5-LUMO+6 ( $e_u$ , **5**) or LUMO+4-LUMO+5 ( $e_u$ , **7**), and HOMO-3 ( $b_{1u}$ )  $\rightarrow$  LUMO+4 ( $b_{2g}$ , **5**) or LUMO+3 ( $b_{2g}$ , **7**) single-electron excitations. The TDDFT predicted NIR transitions in fully conjugated nanobarrels **6** and **8** were found to be  $\sim$ 100 nm shifted to the lower energies compared to the non-conjugated nanobarrels **5** and **7**. The first low-energy  $^1E_u$  excited state in conjugated nanobarrels **6** (713 nm) and **8** (668 nm) is dominated by HOMO ( $b_{1u}$ )  $\rightarrow$  LUMO+2-LUMO+3 ( $e_g$ , **6**) or LUMO+5-LUMO+6 ( $e_g$ , **8**) and HOMO-1-HOMO-2 ( $e_g$ )  $\rightarrow$  LUMO ( $b_{2u}$ , **6**) or LUMO+1 ( $b_{2u}$ , **8**) single-electron excitations, which, in the case of nanobarrel **8**, is also complimented by contributions from HOMO-1-HOMO-2 ( $e_g$ )  $\rightarrow$  LUMO+7 ( $a_{2u}$ ) and HOMO-3 ( $a_{1u}$ )  $\rightarrow$  LUMO+5-LUMO+6 ( $e_g$ ) transitions. The lowest-energy  $^1A_{2u}$  excited state in these systems was predicted at 668 nm (**6**) and 740 nm (**8**) and is dominated by the HOMO ( $b_{1u}$ )  $\rightarrow$  LUMO+1 ( $b_{2g}$ , **6**) or LUMO ( $b_{2g}$ , **8**) single-electron excitations complimented by the HOMO-1-HOMO-2 ( $e_g$ )  $\rightarrow$  LUMO+4-LUMO+5 ( $e_u$ , **6**) or LUMO+2-LUMO+3 ( $e_u$ , **8**). Similar to the nanocages **1** - **4**, conjugation in nanobarrels **6** and **8** results in a significant increase in TDDFT-predicted intensities for the low-energy transitions compared to their non-conjugated analogues **5** and **7**. Another interesting TDDFT prediction on nanobarrels **5** - **8** is that the energy of the first  $^1A_{2u}$  excited state in **8** is lower compared to the lowest energy  $^1E_u$  excited state, while reverse situation is observed in nanobarrels **5** - **7**. Finally, in the case of subtetraazaporphyrin based nanocages **9** and **10**, TDDFT predicted a similar trend

(Figure 13). Indeed, the lowest energy symmetry-allowed triply degenerate  ${}^1T_{1u}$  excited state at 417 nm for the non-conjugated nanocage **9** correlates well with the UV-vis spectrum of the subtetraazaporphyrin. On the other hand, the low energy symmetry allowed triply degenerate  ${}^1T_{1u}$  excited state in the nanocage **10** is  $\sim 100$  nm shifted to the low energy region. The nature of the lowest-energy  ${}^1T_{1u}$  excited state in **9** and **10**, however, are quite different. In the case of non-conjugated nanocage **9**, it consists of by nearly equivalent contributions from HOMO ( $a_{1u}$ )  $\rightarrow$  LUMO+5-LUMO+7 ( $t_{1g}$ ), HOMO-4-HOMO-6 ( $t_{2u}$ )  $\rightarrow$  LUMO-LUMO+1 ( $e_g$ ), and HOMO-1-HOMO-3 ( $t_{1g}$ )  $\rightarrow$  LUMO+2-LUMO+4 ( $t_{1u}$ ) single-electron excitations, while in the case of fully conjugated nanobarrel **10**, it is dominated by the HOMO ( $a_{2g}$ )  $\rightarrow$  LUMO+5-LUMO+7 ( $t_{2u}$ ) single-electron transitions complimented by the HOMO-1-HOMO-3 ( $t_{2u}$ )  $\rightarrow$  LUMO-LUMO+2 ( $t_{2g}$ ) excitations. One of the most exciting TDDFT predictions is that the oscillator strengths for the low-energy transitions for nanostructures **1** - **10** is significantly higher than the individual chromophoric fragments which translates into enormous increase of the molar extinction coefficients of these bands. Another interesting observation is that in nanostructures **1** - **10** TDDFT predicts an unprecedented high intensity band  $\sim 300$  nm. In general, TDDFT-predicted energies for symmetry allowed  $Q$ -band type transitions varied between 417 and 751 nm, which shows optical spectra tunability range across three proposed designs. Finally, due to the symmetry-based selection rules, TDDFT predicted energies in the far NIR region of the nanostructures **1** - **10** are symmetry forbidden and should not be observed in their NIR UV-vis spectra.

## Methane gas adsorption

In order to estimate gas adsorption we arranged our structures in a molecular crystal form. The cubic cell for the single molecules was selected and the lattice parameters were calculated using the periodic density functional calculations. The optimized parameters of unit cells are listed in Table S2. The periodic structures of proposed molecular crystals have two spaces in which gas molecules may adsorb inside and outside cavities as shown in Figure S20. It can be seen that the conjugated configuration forms larger outside pores (see Figure S20b) which can explain the higher adsorption ability of conjugated nanostructures at high pressure.

The calculated methane adsorption isotherms at room temperature (298 K) for all nanostructures are shown in Figures 14 - 16 and Supporting Information Figure S21. The simulation results showed that the methane storage capacities for nanostructures **1**, **2**, **5**, **6**, and **9** exceed and for structures **3**, **4**, and **10** are close to the DOE target  $180 \text{ cm}^3(\text{STP})/\text{cm}^3$  at pressure of 3.5 MPa.<sup>[34]</sup> Only nanobarrels **7** and **8** were found to have a significantly lower methane adsorption capacities at standard DOE conditions. The maximum values of  $256 \text{ cm}^3(\text{STP})/\text{cm}^3$  were estimated for conjugated nanocage **4** and conjugated nanobarrel **6** ( $254 \text{ cm}^3 (\text{STP})/\text{m}^3$ ). Except **8**, the conjugated structures exhibit larger adsorption abilities as compared with non-conjugated ones. The main-group element subtetraazaporphyrin nanocages **9** and **10** show the same tendency but only at pressure up to 2 MPa. Increasing the pressure switched the storage amount that attributed to interaction of  $\text{CH}_4$  molecule with specific adsorption sites at higher methane concentration. At higher pressure, conjugated nanocage structures **2** and **4**, which have slightly larger pores than counterparts **1** and **3**, have larger capacities for methane storage.

It is obvious that the nanobarrels **5** - **8** can be viewed as the smallest building blocks for functional nanotubes. Indeed, these nanobarrels can be converted to continuous 3D tube

structures by removing hydrogen atoms and making direct bonds between carbon atoms of neighboring barrel blocks. These direct connections between the units in functional systems **5t** - **8t**, reduced the macrocycle-to-macrocycle distances along nanotubes (Figure 17) and thus one can expect increased methane storage for all four nanotubes **5t** - **8t** compared to the corresponding nanobarrels **5** - **8**. The adsorption isotherm of methane in **5** - **8** nanostructures for both nanobarrel (**5** - **8**) and nanotube (**5t** - **8t**) configurations are presented in Figures 15a and 15b, respectively. In the case of structure **6**, such modification improves methane adsorption significantly from  $191.2 \text{ cm}^3(\text{STP})/\text{cm}^3$  to  $215 \text{ cm}^3(\text{STP})/\text{cm}^3$ . This value is very close to the maximum experimental value of  $230 \text{ cm}^3(\text{STP})/\text{cm}^3$  observed for Cu-based MOF.<sup>[46]</sup> The systems with smaller volume sizes reach the saturation level of gas sorption at lower pressures and the structures with larger radii can accumulate a higher methane amount at higher pressure. Thus, the continuous tube configuration of conjugated structure **8** with the largest pore diameter shows the largest value of methane adsorption ( $264.2 \text{ cm}^3(\text{STP})/\text{cm}^3$ ) at high pressure (Figure 15b). The adsorption values are also depended on the morphology of the surface. Thus, in the case of non-conjugated structure **5** with minimal pore radius, the formation of the nanotube configuration improve adsorption ability only at low pressures as shown in Figures 15a and 15b.

Although during the MD simulation calculations structures **1** - **10** and **5t** - **8t** become slightly deformed, the micropore volumes do not change significantly for most of them. It can be seen that after optimization at 300 K the methane adsorption isotherms are quite similar to those obtained for the initial structures as shown in Figures S22 - S25. The values of methane uptake before and after *ab initio* MD optimization are presented in Table 2. The largest reduction of methane adsorption was observed in nanobarrel **5** in which bending deformation along the *z* axis was found (see Figure S2). In the case of nanocage **1**, the lower adsorption ability may attribute

to shrinking of the cavity space due to interaction between opposite monomers that leads to the structural strain in the bridging  $sp^3$  carbon groups (see Figure S1). Increasing the distance between monomers in nanocage **3** reduces such strain and the cage volume remains the same. For nanocage **9**, the methane adsorption slightly increase due to the increasing volume of the cavity. Thus, it may be concluded that the symmetry constraints do not affect the adsorption properties of the proposed structures.

**Table 2.** Methane uptake ( $\text{cm}^3(\text{STP})/\text{cm}^3$ ) at  $T=298$  K and different pressure. The values after MD optimization are presented in parentheses.

<i>Structure</i>	<b>Pressure</b>					
	1 PMa	5 MPa	20 MPa	35 MPa	50 MPa	100 MPa
<b>1</b>	37.698 (37.129)	91.439 (84.879)	158.795 (142.552)	183.108 (165.249)	196.481 (176.901)	215.494 (197.002)
<b>2</b>	40.400 (40.851)	95.328 (95.015)	166.838 (171.383)	193.561 (198.455)	206.345 (213.478)	232.559 (240.567)
<b>3</b>	11.393 (11.586)	51.907 (52.517)	133.934 (134.421)	170.973 (171.363)	191.687 (192.618)	227.726 (229.888)
<b>4</b>	8.506 (9.252)	39.575 (42.284)	121.242 (122.866)	168.527 (169.843)	201.324 (200.567)	255.768 (255.372)
<b>5b</b>	18.009 (19.812)	70.415 (62.017)	155.706 (126.477)	188.336 (153.280)	205.626 (170.071)	232.017 (197.055)

<b>5t</b>	26.474 (25.574)	93.662 (91.916)	163.906 (165.339)	185.938 (189.180)	197.834 (202.980)	220.465 (228.286)
<b>6b</b>	12.449 (13.795)	54.945 (57.609)	145.990 (146.570)	191.155 (186.525)	214.828 (210.571)	253.730 (250.403)
<b>6t</b>	20.927 (19.44)	90.571 (83.068)	186.928 (176.619)	215.705 (208.069)	233.120 (224.306)	255.957 (251.744)
<b>7b</b>	5.665 (6.042)	26.959 (28.210)	90.736 (92.248)	138.761 (140.018)	174.955 (175.329)	244.413 (242.791)
<b>7t</b>	10.941 (9.989)	51.880 (47.707)	144.853 (138.941)	185.854 (180.948)	209.928 (206.525)	247.665 (244.848)
<b>8b</b>	3.685 (3.603)	17.869 (17.352)	65.277 (63.279)	105.700 (103.061)	140.328 (138.045)	228.070 (224.856)
<b>8t</b>	7.094 (6.791)	34.838 (32.661)	119.064 (111.788)	173.287 (164.099)	207.223 (199.193)	264.184 (257.368)
<b>9</b>	40.526 (45.190)	106.387 (110.524)	158.685 (168.620)	179.942 (188.745)	193.020 (202.337)	218.002 (225.997)
<b>10</b>	76.444 (75.118)	136.124 (138.244)	168.357 (171.056)	177.292 (180.182)	183.738 (185.854)	194.518 (194.911)

In the cases of nanostructures **1 - 3**, **5**, **6**, **9** and **10**, as well as **5t - 8t** the obtained values surpass the uptake value of methane in experimentally synthesized metal organic framework (MOF) structure, PCN-11, ( $\text{Cu}_2(\text{sbtc})$ , sbtc = *trans*-stilbene-3,3',5,5'-tetracarboxylate) that exhibit  $171 \text{ cm}^3(\text{STP})/\text{cm}^3$  at 298 K and 3.5 MPa.<sup>[47]</sup> To the best of our knowledge, two MOF structures,  $\text{Ni}_2(\text{dhtp})$ , (dhtp = 2,5-dihydroxyterephthalate)<sup>[48]</sup> and  $\text{Cu}_2(\text{adip})$ , (5,5'-(9,10-anthracenediyl)diisophthalic acid) mentioned before<sup>[46]</sup> show the excellent methane adsorption capacity of  $190 \text{ cm}^3(\text{STP})/\text{cm}^3$  and  $230 \text{ cm}^3(\text{STP})/\text{cm}^3$  at 298 K and 3.5 MPa, respectively. In these structures, the unsaturated Ni and Cu ions contribute significantly in gas adsorption. Indeed the  $\text{Zn}_2(\text{dhtp})$  structure<sup>[48]</sup> yield excess methane adsorption capacities around  $170 \text{ cm}^3(\text{STP})/\text{cm}^3$  and this is a lower value as compared with the Zn-based structures studied here. Thus, one possible way to increase the capacity of our structures in the future may lie in the substitution of the Zn ions by Cu ones.

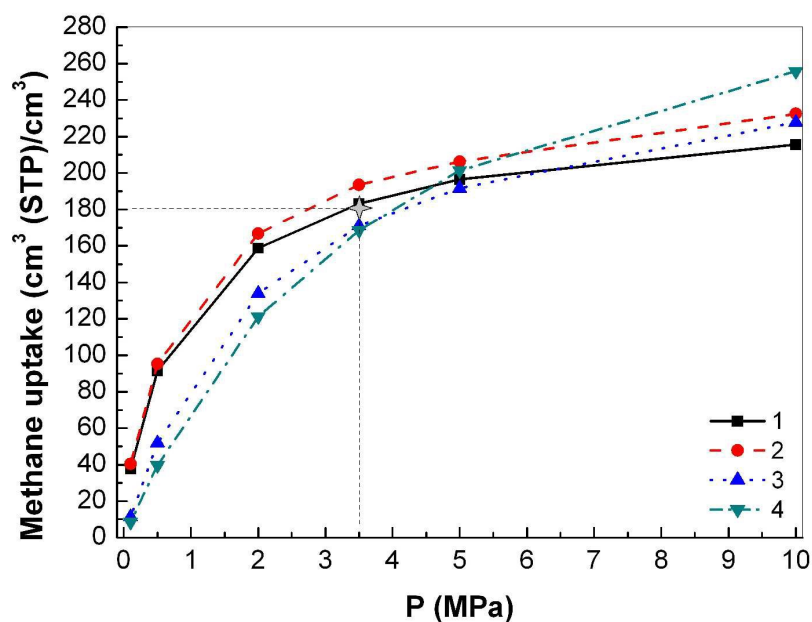


**Figure 14.** Adsorption isotherm of CH<sub>4</sub> in nanostructures **1** - **4** at T=298 K. Four-point star indicates the DOE target.<sup>[34]</sup>

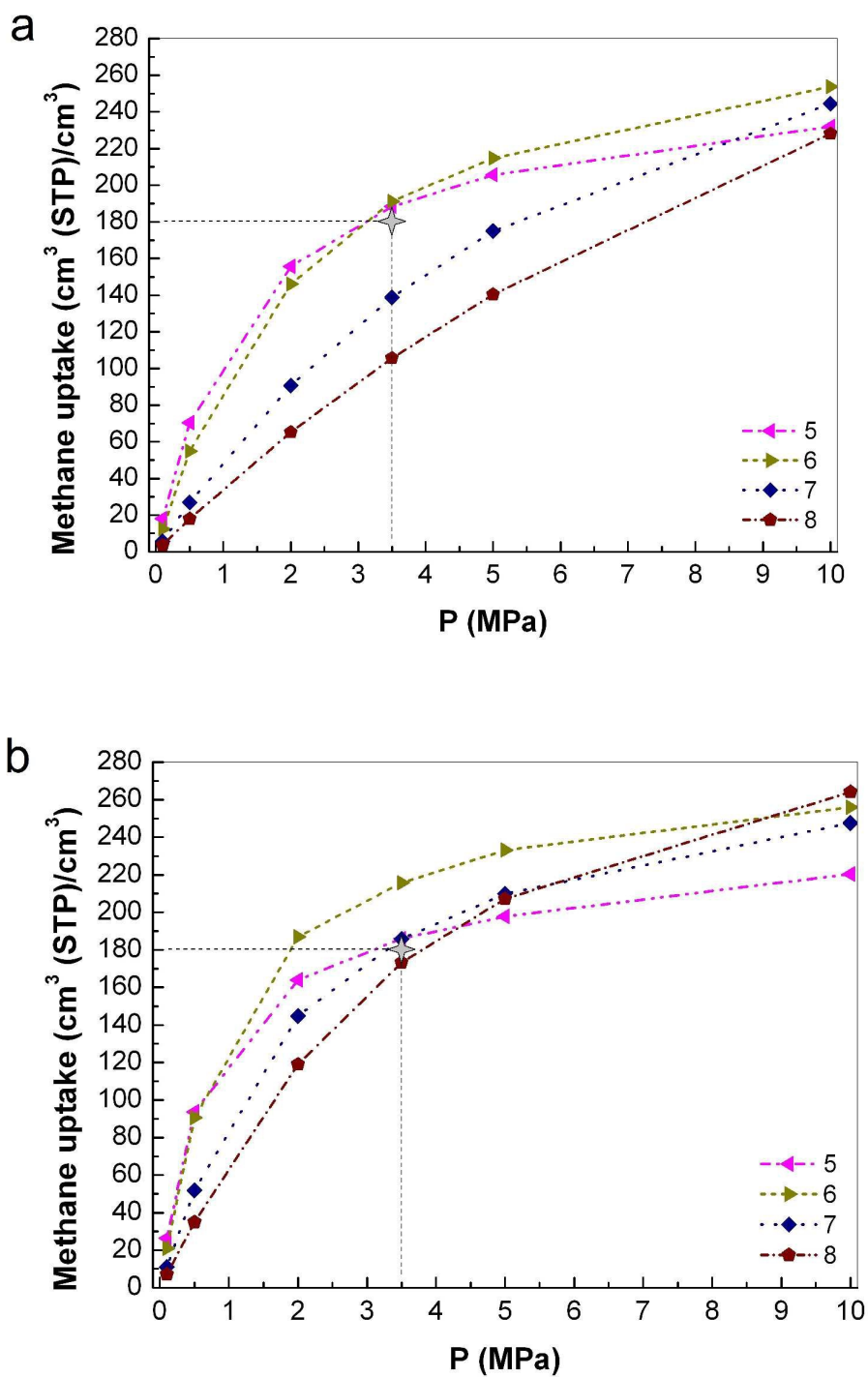


**Figure 15.** Adsorption isotherm of CH<sub>4</sub> in nanostructures **5 - 8** (a) and **5t - 8t** (b) at T=298 K.

Four-point star indicates the DOE target.<sup>[34]</sup>

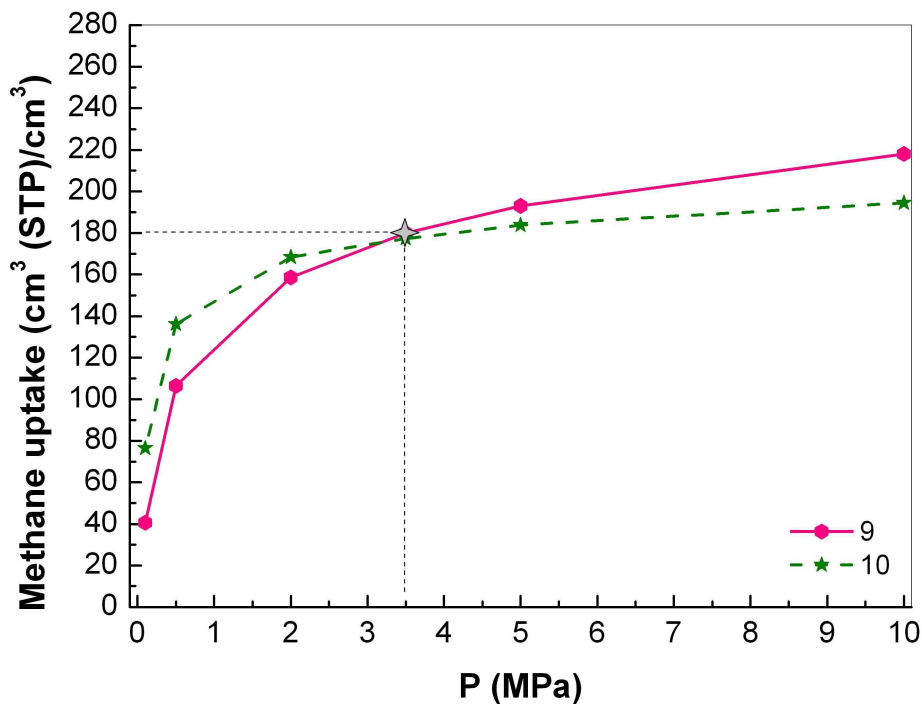


**Figure 16.** Adsorption isotherm of CH<sub>4</sub> in nanostructures **9 - 10** at T=298 K. Four-point star

indicates the DOE target.<sup>[34]</sup>

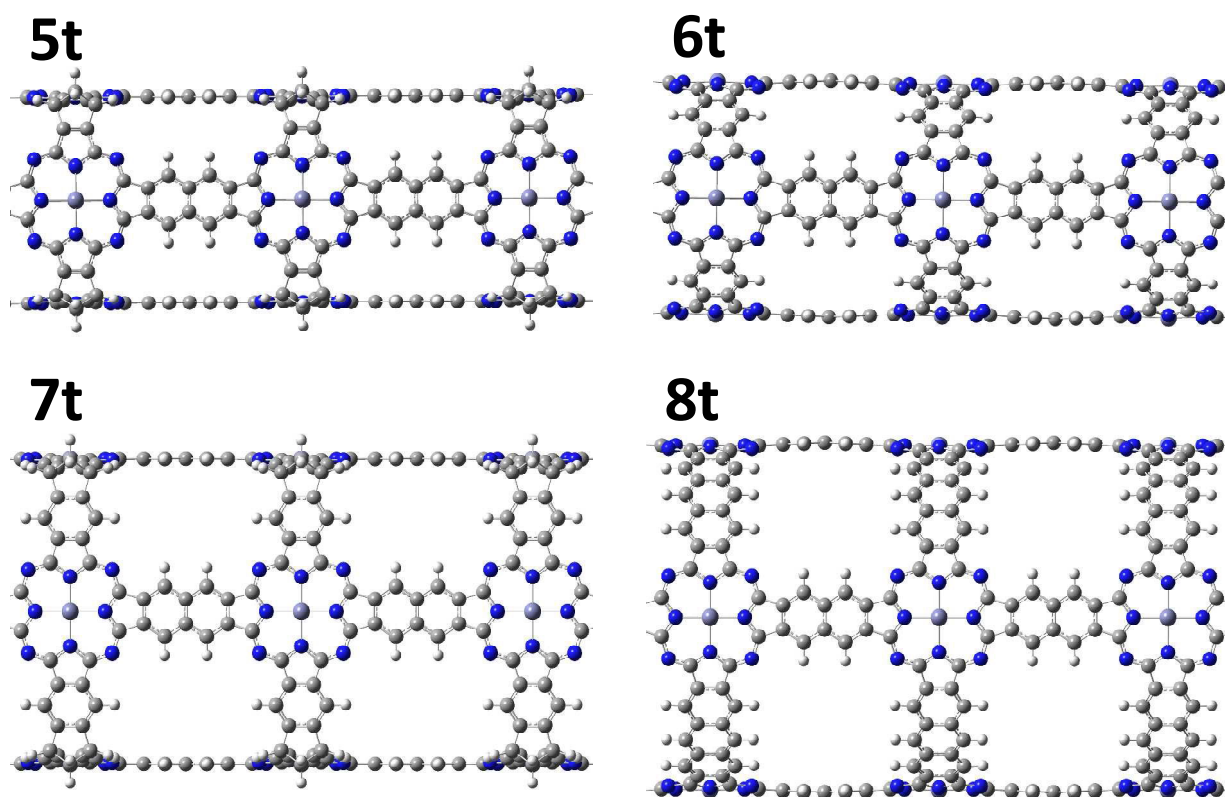


**Figure 17.** Functional nanotubes **5t** - **8t** formed by translation of nanobarrells **5** - **8**.

In comparison with the pure nano-carbon structures such as fullerenes and nanotubes, the walls in the proposed structures **1** - **10** contain ordered holes due to the specific geometry of the corresponding building blocks. Such peculiarity opens the possibility to adsorb small molecules not only inside (blue cycle) and outside (red cycle) of the nano-structures **1** - **10** but also in intermediates spaces (green cycles) as shown in Figures S26 - S39. The following trends in adsorption of methane gas were observed, which correlate well with the structural motif in **1** - **10**: (i) at the low pressure the methane molecules adsorb inside the cage for all structures; (ii) with pressure increase, the outside and intermediate voids start to adsorb a methane gas. This effect can be explained by the interaction between a guest molecule and a host framework which is essentially affected the adsorption behavior at low pressure. This weak interaction is strongly

depends on a number of surface atoms located closely to adsorbed molecules. In our case all structures have curved configurations and hence the concave and convex geometries of the interior and exterior surfaces, respectively. Thus, for interior space the interaction between methane and host frameworks is stronger in comparison to an interaction of methane outside of nanocages, nanobarrels, and nanotubes. Moreover, the structures with smaller diameter show the higher adsorption ratio at low pressure that also related to larger interaction of methane with surface atoms. This is in agreement with *ab initio* analysis of interaction between small molecules, H<sub>2</sub> and CO with carbon nanotubes performed recently.<sup>[49]</sup>

Since the diameter of the outside space is larger for conjugated systems, the adsorption ratio between the outside and intermediate spaces is higher for these structures. It is interesting to mention that the intermediate space plays an important role in the adsorption process for the non-conjugated structures with small diameters (**1** and **5**). During the MD optimization, the structural deformation leads to the elimination of the regularity of intermediate spaces and this affects the adsorption process. The formation of a regular nanotube from nanobarrel **5** removes such deformations and the value of methane uptake remains the same as shown in Table 2 and Figure S24a. Thus, the presence of intermediate spaces is an important feature of the proposed structures **1** - **10** which gives them a significant advantage over the well-known carbon or BN nanostructures since the inside and outside volumes are not isolated. Moreover, it helps to simplify the technology of sorption/desorption procedures.

The proposed nanostructures have additional features that play an important role in the methane gas adsorption process. The proposed structures may consider as one of the types of carbon-based (carbonaceous) materials. These materials recently take a lot of scientific interest as the state-of-the-art of carbon-based adsorbent that may apply for effective, clean and low energy

requirement storage/separation process.<sup>[50]</sup> Among various strategies that improve the adsorption properties of carbonaceous materials, N-doping, surface functionalization and extra-framework ions can be selected as the most commonly ones. In the case of nitrogen doping the concentration as well as nitrogen effect on the long-term stability of microporous carbons need to be controlled. In our case, the nitrogen concentration is high and stable because it nitrogen chemically involved inside the molecular building blocks.

## **Discussion**

Overall, we have designed three key motifs of the functional nanostructures based on tetraazaporphyrin subunits. These include fully conjugated (systems **2**, **4**, **6**, **8**, and **10**), as well as, saturated bridge interrupted (systems **1**, **3**, **5**, **7**, and **9**) geometries. The potential applications of these new conceptual nanostructures **1** - **10** can be centered around their optical, redox, and topology properties which can be tuned up by the size, topology, and conjugation. For instance, the diameter of pores in nanosystems **1** - **10** can vary between 1.35 and 4.71 Å which can be used for selective separation of simple polyatomic molecules. Indeed, the pore diameter in all nanostructures is good enough to facilitate methane gas storage or, in the case of the subtetraazaporphyrin-based cages **9** and **10**, one might expect that larger polyatomic molecules such as methane or carbon dioxide could be accommodated inside of the nanocage. The change of the non-conjugated links by conjugated fragments in nanostructures **1** - **10** destabilizes the energies of the HOMO orbitals and thus can tune up the first oxidation potential of the nanosystem. Such tunability of the first oxidation potential is critical for applications of the transition metal analogues of nanostructures **1** - **8** in a variety of catalytic reactions, which

involves activation of small polyatomic molecules such as hydrogen, oxygen, carbon dioxide, or methane. Our TDDFT calculations demonstrate that by varying the degree of conjugation and the type of the chromophore in the nanocage or nanobarrel we can easily adjust the low energy transitions between 417 and 751 nm thus covering the majority of the solar spectrum. Taking into consideration that TDDFT predicts cooperative effect in the intensity of these transitions, proposed nanostructures may also potentially be used as quantum dot analogues for solar cells and imaging/bio-imaging applications. Indeed, one might expect that the nanostructures **1 - 10** may have lower toxicity similar to the regular phthalocyanines and their analogues, which are currently used in the photodynamic therapy of cancer. Such low expected toxicity is in contrast to the CdSe and CdTe quantum dots, which are used for *in vitro* and *in vivo* bio-imaging and solar energy conversion. In addition, all proposed nanostructures effectively adsorb methane gas molecules with a majority of compounds being close or exceeding DOE target of  $180 \text{ cm}^3 \text{ (STP)} / \text{cm}^3$  for material-based methane storage at room temperature. The possibility of introduce various metal ions inside porphyrins may enhance the interaction with polarizable molecules such as CO or CO<sub>2</sub>. This feature may be considered in the case of CO/N<sub>2</sub> or CO<sub>2</sub>/CH<sub>4</sub> separation processes and will be a subject of future research. Therefore, in addition to 3D nanostructures such as fullerenes and nanotubes, new functional 3D nanomaterials such as nanostructures **1 - 10** would provide a new direction in nanoscience.

### **ASSOCIATED CONTENT**

**Supporting information.** Coordinates for DFT optimized structures. DFT predicted energies and frontier orbitals. This material is available free of charge via the Internet at

<http://pubs.acs.org>.

### **ACKNOWLEDGEMENTS**

RVB is grateful for the support of the HITACHI SR16000-M1 supercomputing facility by the Computer Science Group and E-IMR center at the Institute for Materials Research, Tohoku University, Sendai. Generous support from the NSF CHE-1401375, CHE-1464711, and Minnesota Supercomputing Institute to VN is greatly appreciated. This work was partially supported by ICC-IMR of Tohoku University.

### AUTHOR INFORMATION

#### **Corresponding Author**

\*rodion@imr.tohoku.ac.jp (RVB) and \*vnemykin@d.umn.edu (VNN)

**REFERENCES**

- 1 (a) P. A. Alivisatos, *ACS Nano* 2008, **2**, 1514; (b) I. Kalashnikova, S. Das and S. Seal, *Nanomedicine* 2015, **10**, 2593-2612; (c) K. Rani, *Int. J. Pharma Res. Health Sci.* 2014, **2**, 197-202; (d) J. M. Abendroth, O. S. Bushuyev, P. S. Weiss and C. J. Barrett, *ACS Nano* 2015, **9**, 7746-7768; (e) L. Wang and G. Arrabito, *Analyst* 2015, **140**, 5821-5848.
- 2 (a) R. U. Palekar, A. P. Jallouk, G. M. Lanza, H. Pan and S. A. Wickline, *Nanomedicine* 2015, **10**, 1817-1832; (b) D. W.-C. Chen and S.-J. Liu, *Nanomedicine* 2015, **10**, 1959-1971; (c) D. Elbrecht, J. Mitchell, A. Lekey, K. Marquardt, K. Knight, J. Smith and R. DeLong, *Rev. Nanoscience Nanotechnology* 2013, **2**, 365-381; (d) H. Homayoni, L. H. Rashidi and W. Chen, *Rev. Nanoscience Nanotechnology* 2014, **3**, 107-132; (e) E. McLeod, Q. Wei and A. Ozcan, *Anal. Chem.* 2015, **87**, 6434-6445.
- 3 (a) H. W. Kroto, H. R. Heath, S. C. O'Brien, R. F. Curl and R. E. Smalley, *Nature* 1985, **318**, 162; (b) Y. Zheng, Y. Jiao and S. Z. Qiao, *Adv. Mater.* 2015, **27**, 5372-5378; (c) Y.-Y. Huang, S. K. Sharma, T. Dai, H. Chung, A. Yaroslavsky, M. Garcia-Diaz, J. Chang, L. Y. Chiang and M. R. Hamblin, *Nanotechnology Rev.* 2012, **1**, 111-146; (d) D. Nagda, K. S. Rathore, M. Bharkatiya, S. S. Sisodia and R. K. Nema, *J. Chem. Pharm. Res.* 2010, **2**, 240-248; (e) S. R. Stoyanov, A. V. Titov and P. Kral, *Coord. Chem. Rev.* 2009, **253**, 2852-2871.
- 4 (a) S. Iijima, *Nature* 1991, **354**, 56; (b) A. Husen and K. S. Siddiqi, *J. Nanobiotechnology* 2014, **12**, 16/1-16/19; (c) S. Jayronia, A. Hardenia and S. Jain, *World J. Pharm. Res.* 2014,

- 3, 295-310; (d) A. Kahru and A. Ivask, *Acc. Chem. Res.* 2013, **46**, 823-833; (e) J. Cabaj and J. Soloducho, *Mater. Sci. Applicat.* 2014, **5**, 752-766; (f) E. Munoz-Sandoval, *J. Nanoparticle Res.* 2014, **16**, 2152/1-2152/22; (g) K.-W. Ng, W.-H. Lam and S. Pichiah, *Renew. Sustainable Energy Rev.* 2013, **28**, 331-339.
- 5 (a) K. S. Novoselov, A. K. Geim, S. V. Morozov, D. Jiang, Y. Zhang, S. V. Dubonos, I. V. Grigorieva and A. A. Firsov, *Science* 2004, **306**, 666; (b) S. Kumar, W. Ahlawat, R. Kumar and N. Dilbaghi, *Biosensors & Bioelectronics* 2015, **70**, 498-503; (c) L. A. Chernozatonskii, P. B. Sorokin and A. A. Artukh, *Russ. Chem. Rev.* 2014, **83**, 251-279; (d) M. Caffo, L. Merlo, D. Marino and G. Caruso, *Nanomedicine* 2015, **10**, 615-625; (e) Q. Peng, A. K. Dearden, J. Crean, L. Han, S. Liu, X. Wen and S. De, *Nanotechnology, Sci. Appl.* 2014, **7**, 1-29; (f) J. Yang, M. Ma, L. Li, Y. Zhang, W. Huang and X. Dong, *Nanoscale* 2014, **6**, 13301-13313; (g) K. Muellen, *ACS Nano* 2014, **8**, 6531-6541; (h) R. Ramachandran, V. Mani, S.-M. Chen, S. Ramiah and B.-S. Lou, *Int. J. Electrochem. Sci.* 2013, **8**, 11680-11694.
- 6 *Carbon Nanotubes Science and Applications*; Meyyappan, M., Ed.; CRC Press: New York, 2005.
- 7 (a) X. Lu, M. Zhang, D. Jin, Y. Dang, S. Zhou, S. Wei, H. Zhu and L. Zhao, *Mater. Lett.* 2015, **161**, 545-548; (b) G. Moussa, C. Salameh, A. Bruma, S. Malo, U. B. Demirci, S. Bernard and P. Miele, *Inorganics* 2014, **2**, 396-409; (c) W. Meng, Y. Huang, Y. Fu, Z. Wang and C. Zhi, *J. Mater. Chem. C* 2014, **2**, 10049-10061; (d) K. Raidongia, A. Gomathi and C. N. R. Rao, *Isr. J. Chem.* 2010, **50**, 399-404; (e) D. Golberg, Y. Bando, O. Stéphan and K. Kurashima, *Appl. Phys. Lett.* 1998, **73**, 2441-2443; (f) Y. F. Zhukovskii, S. Piskunov, N. Pugno, B. Berzina, L. Trinkler and S. Bellucci, *J. Phys. Chem. Solids* 2009, **70**, 796-803;

- (g) D. Golberg, Y. Bando, M. Eremets, K. Takemura, K. Kurashima and H. Yusa, *Appl. Phys. Lett.* 1996, **69**, 2045-2047; (h) N. G. Chopra, R. J. Luyken, K. Cherrey, V. H. Crespi, M. L. Cohen, S. G. Louie and A. Zettl, *Science* 1995, **269**, 966-967.
- 8 (a) N. Sakhavand and R. Shahsavari, *ACS Appl. Mater. Interfaces* 2015, **7**, 18312-18319; (b) Z. Jacob, *Nature Mater.* 2014, **13**, 1081-1083; (c) A. Pakdel, C. Zhi, Y. Bando and D. Golberg, *Mater. Today* 2012, **15**, 256-265; (d) A. M. Seayad and D. M. Antonelli, *Adv. Mater.* 2004, **16**, 765-777; (e) F. Jensen and H. Toftlund, *Chem. Phys. Lett.* 1993, **201**, 89-96.
- 9 (a) F. Zhao, Y. Wang, M. Zhu and L. Kang, *RSC Adv.* 2015, **5**, 56348-56355; (b) Y. Jia,; H. Zhao, Q. Guo, X. Wang, H. Wang and F. Xia, *ACS Photonics* 2015, **2**, 907-912; (c) A. Pakdel, Y. Bando and D. Golberg, *Chem. Soc. Rev.* 2014, **43**, 934-959; (d) Y. Lin and J. W. Connell, *Nanoscale* 2012, **4**, 6908-6939; (e) V. V. Pokropivny and A. L. Ivanovskii, *Russ. Chem. Rev.* 2008, **77**, 837-873; (f) H. Terrones and M. Terrones, *New J. Phys.* 2003, **5**, 1-37; (g) H. Terrones, M. Terrones and J. L. Moran-Lopez, *Curr. Sci.* 2001, **81**, 1011-1029.
- 10 (a) A. Kasuya, R. Sivamohan, Y. A. Barnakov, I. M. Dmitruk, T. Nirasawa, V. R. Romanuk, V. Kumar, S. V. Mamykin, K. Tohji, V. Jeyadevan, K. Shinoda, T. Kudo, O. Terasaki, Z. Liu, R. V. Belosludov, V. Sundararajan and Y. Kawazoe, *Nature Mater.* 2004, **3**, 99-102; (b) A. Kasuya, Y. Noda, I. Dmitruk, V. Romanyuk, Y. Barnakov, K. Tohji, V. Kumar, R. Belosludov, Y. Kawazoe and N. Ohuchi, *Eur. Phys. J. D* 2005, **34**, 39-41; (c) S. Botti and M. A. L. Marques, *Phys. Rev B* 2007, **75**, 035311/1-035311/6; (d) S. Kudera, M. Zanella, C. Giannini, A. Rizzo, Y. Li, G. Gigli, R. Cingolani, G. Ciccarella, W. Spahl, W. J. Parak and L. Manna, *Adv. Mater.* 2007, **19**, 548-552; (e) E. Kucur, J. Ziegler and T. Nann, *Small* 2008, **4**, 883-887; (f) F. S. Riehle, R. Bienert, R. Thomann, G. A. Urban and M. Krueger, *Nano Lett.* 2009, **9**, 514-518; (g) V. R. Romanyuk, I. M. Dmitruk, Yu. A. Barnakov, R. V.

- Belosludov and A. Kasuya, *J. Nanosci. Nanotech.* 2009, **9**, 2111-2118; (h) Y.-S. Park, A. Dmytruk, I. Dmitruk, A. Kasuya, M. Takeda, N. Ohuchi, Y. Okamoto, N. Kaji, M. Tokeshi and Y. Baba, *ACS Nano* 2010, **4**, 121-128; (i) Z.-J. Jiang and D. F. Kelley, *ACS Nano* 2010, **4**, 1561-1572; (k) K. A. Nguyen, P. N. Day and R. Pachter, *J. Phys. Chem. C* 2010, **114**, 16197-16209; (m) Y. Wang, Y. Zhang, F. Wang, D. E. Giblin, J. Hoy, H. W. Rohrs, R. A. Loomis and W. E. Buhro, *Chem. Mater.* 2014, **26**, 2233-2243.
- 11 (a) Y. Wang, Y. Zhou, Y. Zhang and W. E. Buhro, *Inorg. Chem.* 2015, **54**, 1165-1177; (b) P. Han and G. Bester, *Phys. Rev. B.* 2012, **85**, 041306/1-041306/4; (c) R. Sathyamoorthy, P. Sudhagar, R. S. Kumar and T. M. Sathyadevan, *Cryst. Res. Technol.* 2010, **45**, 99-103; (d) V. I. Emel'yanov, A. Baidullaeva, A. I. Vlasenko, L. F. Kuzan, O. S. Lytvyn and P. E. Mozol', *Tech. Phys. Lett.* 2006, **32**, 732-734; (e) M. W. DeGroot, N. J. Taylor and J. F. Corrigan, *J. Mater. Chem.* 2004, **14**, 654-660; (f) S. Namsani, N. N. Nair and J. K. Singh, *J. Comput. Chem.* 2015, **36**, 1176-1186; (g) G. Mallocci, L. Chiodo, A. Rubio and A. Mattoni, *J. Phys. Chem. C* 2012, **116**, 8741-8746; (h) A. Mohajeri, M. Alipour and M. B. Ahmadi, *Chem. Phys. Lett.* 2011, **503**, 162-166; (i) S. Pal, B. Goswami and P. Sarkar, *J. Phys. Chem. C* 2008, **112**, 6307-6312.
- 12 (a) K. Yoosaf, J. Iehl, I. Nierengarten, M. Hmadeh, A.-M. Albrecht-Gary, J.-F. Nierengarten and N. Armaroli, *Chem. Eur. J.* 2014, **20**, 223-231; (b) Z. S. Yoon, J. Yang, H. Yoo, S. Cho and D. Kim, in: *Handbook of Porphyrin Science* K. M. Kadish, K. M. Smith, R. Guilard, (Eds.) 2010, **1**, 439-505; (c) A. D'Urso, M. E. Fragala and R. Purrello, *Chem. Commun.* 2012, **48**, 8165-8176; (d) H.-W. Wang, C.-H. Chen, T.-S. Lim, S.-L. Huang and T.-Y. Luh, *Chem. Asian J.* 2011, **6**, 524-533; (e) B. Ventura, L. Flamigni, M. Beyler, V. Heitz and J.-P. Sauvage, *Chem. Eur. J.* 2010, **16**, 8748-8756; (f) R. F. Kelley, W. S. Shin, B. Rybtchinski,

- L. E. Sinks and M. R. Wasielewski, *J. Am. Chem. Soc.* 2007, **129**, 3173-3181; (g) A. Satake, O. Shoji and Y. Kobuke, *J. Organometallic Chem.* 2007, **692**, 635-644; (h) S. A. L. Rousseaux, J. Q. Gong, R. Haver, B. Odell, T. D. W. Claridge, L. M. Herz and H. L. Anderson, *J. Am. Chem. Soc.* 2015, **137**, 12713-12718; (i) C. E. Tait, P. Neuhaus, M. D. Peeks, H. L. Anderson and C. R. Timmel, *J. Am. Chem. Soc.* 2015, **137**, 8284-8293; (j) P. Neuhaus, A. Clossen, J. Q. Gong, L. M. Herz and H. L. Anderson, *Angew. Chem., Int. Ed.* 2015, **54**, 7344-7348; (k) C. E. Tait, P. Neuhaus, H. L. Anderson and C. R. Timmel, *J. Am. Chem. Soc.* 2015, **137**, 6670-6679; (l) J. Q. Gong, P. Parkinson, D. V. Kondratuk, G. Gil-Ramirez, H. L. Anderson and L. M. Herz, *J. Phys. Chem. C* 2015, **119**, 6414-6420; (m) V. N. Nemykin and E. A. Lukyanets, in: *Handbook of Porphyrin Science*, K. M. Kadish, K. M. Smith, R. Guilard (Eds.); World Scientific: Singapore, 2010, **Vol 3**, pp. 1 - 323; (n) E. A. Lukyanets and V. N. Nemykin, *J. Porphyrins Phthalocyanines* 2010, **14**, 1 - 40; (o) V. N. Nemykin and E. A. Lukyanets, *ARKIVOC* 2010, **(i)**, 136-208; (p) N. Kobayashi, A. Muranaka and V. N. Nemykin, *Tetrahedron Lett.* 2001, **42**, 913-915.
- 13 (a) J. W. Buchler and D. K. P. Ng, in: *The Porphyrin Handbook*; K. M. Kadish, K. M. Smith, R. Guilard, (Eds.), Academic Press: San Diego, 2000, **Vol. 3**, pp. 245–294; (b) R. Weiss and J. Fischer, in: *The Porphyrin Handbook*; K. M. Kadish, K. M. Smith, R. Guilard, (Eds.) Academic Press: San Diego, 2003, **Vol. 16**, pp. 171–246; (c) N. Kobayashi, *Coord. Chem. Rev.* 2002, **227**, 129–152; (d) J. Jiang, W. Liu and D. P. Arnold, *J. Porphyrins Phthalocyanines* 2003, **7**, 459–473; (e) J. Jiang, K. Kasuga and D. P. Arnold, in: *Supramolecular Photosensitive and Electroactive Materials*; H.S. Nalwa, (Ed.) Academic Press: New York, 2001, pp. 113–210; (f) V. E. Pushkarev, L. G. Tomilova and Yu. V. Tomilov, *Russ. Chem. Rev.* 2008, **77**, 875–907; (g) J. Jiang and D. K. P. Ng, *Acc. Chem.*

- Res.* 2009, **42**, 79–88; (h) Y. Bian, Y. Zhang, Z. Ou and J. Jiang, in: *Handbook of Porphyrin Science: With Applications to Chemistry, Physics, Materials Science, Engineering, Biology and Medicine*; K. M. Kadish, K. M. Smith, R. Guilard, (Eds.) World Scientific: Singapore, 2011, **Vol. 14**, pp. 249–460.
- 14 (a) F. H. Thomas and A. L. Moser, *The Phthalocyanines: Manufacture and Application*, CRC Press: Boca Raton, 1983, **Vol. 2**, pp. 1 - 364; (b) D. Wöhrle, in: *Phthalocyanines: Properties and Applications*; C. C. Leznoff, A. B. P. Lever, (Eds.) VCH Publishers: Inc. New York, 1989, **Vol. 1**, pp. 55-132; (c) G. Ferraudi, in: *Phthalocyanines: Properties and Applications*; C. C. Leznoff, A. B. P. Lever, (Eds.) VCH Publishers Inc.: New York, 1989, **Vol. 1**, pp. 291-340; (e) M. R. Wasielewski, *Chem. Rev.* 1992, **92**, 435-461; (f) D. Gust, T. A. Moore and A. L. Moore, *Acc. Chem. Res.* 1993, **26**, 198-205.
- 15 (a) J. Cheek and J. H. Dawson, in: *Porphyrin Handbook*, K. M. Kadish, K. M. Smith, R. Guilard, (Eds.) Academic Press: New York, 2000, **Vol. 7**, pp. 339-369; (b) I. Rosenthal and E. Ben-Hur, in: *Phthalocyanines: Properties and Applications*; C. C. Leznoff, A. B. P. Lever, (Eds.) VCH Publishers, Inc.: New York, 1989, **Vol. 1**, pp. 393-425; (c) R. Bonnett, *Chemical Aspects of Photodynamic Therapy*; Gordon and Breach: Amsterdam, 2000; (d) B. Grimm, A. Hausmann, A. Kahnt, W. Seitz, F. Spanig and D. M. Guldi, in: *Handbook of Porphyrin Science*; K. M. Kadish, K. M. Smith, R. Guilard, (Eds.) *World Scientific*; Singapore, 2010, **Vol. 1**, pp. 133 - 219; (e) A. W. Snow and W. R. Barger, in: *Phthalocyanines: Properties and Applications*; C. C. Leznoff, A. B. P. Lever, (Eds.) VCH Publishers, Inc.: New York, 1989, **Vol. 1**, pp. 341-392; (f) M. Jurow, A. E. Schuckman, J. D. Batteas and C. M. Drain, *Coord. Chem. Rev.* 2010, **254**, 2297-2310.

- 16 (a) N. B. McKeown, *Phthalocyanine Materials: Synthesis, Structure and Function*; Cambridge University Press: Cambridge, 1998; (b) D. Dini and M. Hanack, in: *Porphyrim Handbook*; K. M. Kadish, K. M. Smith, R. Guillard, (Eds.) Academic Press: San Diego, 2003, **Vol. 17**, pp. 1-36; (c) M. Wark, in: *Porphyrim Handbook*; K. M. Kadish, K. M. Smith, R. Guillard, (Eds.) Academic Press: San Diego, 2003, **Vol. 17**, pp. 247-284; (d) E. Ben-Hur and W.-H. Chan, in: *Porphyrim Handbook*, K. M. Kadish, K. M. Smith, R. Guillard, (Eds.) Academic Press: San Diego, 2003, **Vol. 19**, pp. 1-36; (e) M. Bouvet, in: *Porphyrim Handbook*; K. M. Kadish, K. M. Smith, R. Guillard, (Eds.) Academic Press: San Diego, 2003, **Vol. 19**, pp. 37-104; (f) V. N. Nemykin, S. V. Dudkin, F. Dumoulin, C. Hirel, A. G. Gurek and V. Ahsen, *ARKIVOC* 2014, (i), 142-204.
- 17 (a) T. Fukuda and N. Kobayashi, in: *Handbook of Porphyrim Science*; K. M. Kadish, K. M. Smith, R. Guillard, (Eds.) World Scientific: Singapore, 2010, **Vol. 9**, pp. 1-644; (b) N. Kobayashi, H. Ogata, N. Nonaka and E. A. Luk'yanets, *Chem. Eur. J.* 2003, **9**, 5123 – 5134.
- 18 (a) R. S. Iglesias, C. G. Claessens, T. Torres, M. Ángeles Herranz, V. R. Ferro and J. M. G. de la Vega, *J. Org. Chem.* 2007, **72**, 2967-2977; (b) E. Orti, J. L. Bredas and C. Clarisse, *J. Chem. Phys.* 1990, **92**, 1228-1235.
- 19 (a) T. V. Duncan, T. Ishizuka and M. J. Therien, *J. Am. Chem. Soc.* 2007, **129**, 9691–9703; (b) A. Tsuda and A. Osuka, *Science* 2001, **293**, 79-82; (c) N. Aratani, D. Kim and A. Osuka, *Chem. Asian J.* 2009, **4**, 1172-1182.
- 20 (a) Y. Yamaguchi, *J. Chem. Phys.* 2005, **122**, 184702/1 - 184702/10; (b) S. Yoshimoto, Y. Honda, O. Ito and K. Itaya, *J. Am. Chem. Soc.* 2008, **130**, 1085-1092; (c) Y. Yamaguchi, *Int. J. Quantum Chem.* 2009, **109**, 1584–1597; (d) Y. Yamaguchi, *J. Chem. Phys.* 2002, **117**, 9688-9694; (e) Y. Yamaguchi, *J. Phys. Chem.* 2004, **120**, 7963-7970.

- 21 (a) G. Zhu, Q. Sun, Y. Kawazoe and P. Jena, *Int. J. Hydrogen Energy* 2015, **40**, 3689-3696;  
(b) J. Zhou, Q. Wang, Q. Sun, Y. Kawazoe and P. Jena, *J. Phys. Chem. Lett.* 2012, **3**,  
3109–3114; (c) Y. Li and Q. Sun, *Scientific Reports* 2014, **4**, 4098.
- 22 G. Zhu, Y. Li, K. Lu and Q. Sun, *ChemPhysChem* 2014, **15**, 126-131.
- 23 A. D. Becke, *J. Chem. Phys.* 1993, **98**, 5648-5652.
- 24 C. Lee, W. Yang and R. G. Parr, *Phys. Rev. B* 1988, **37**, 785-789.
- 25 (a) A. J. H. Wachters, *J. Chem. Phys.* 1970, **52**, 1033; (b) R. Ditchfield, W. J. Hehre and J. A. Pople, *J. Chem. Phys.* 1971, **54**, 724; (c) W. J. Hehre, R. Ditchfield and J. A. Pople, *J. Chem. Phys.* 1972, **56**, 2257.
- 26 (a) O. A. Vydrov and G. E. Scuseria, *J. Chem. Phys.* 2006, **125**, 234109; (b) O. A. Vydrov, J. Heyd, A. Krukau and G. E. Scuseria, *J. Chem. Phys.* 2006, **125**, 074106; (c) P. P. Feher, M. Purgel and F. Joo, *Comput. Theor. Chem.* 2014, **1045**, 113-122; (d) I. H. Nayyar, E. R. Batista, S. Tretiak, A. Saxena, D. L. Smith and R. L. Martin, *J. Polymer Sci. B* 2013, **51**, 935-942; (e) Y. D. Zhao and Y. Liao, *Adv. Mater. Res.* 2011, **322**, 120-124; (f) O. A. Vydrov, G. E. Scuseria and J. P. Perdew, *J. Chem. Phys.* 2007, **126**, 154109.
- 27 M. J. Frisch, G. W. Trucks, H. B. Schlegel, G. E. Scuseria, M. A. Robb, J. R. Cheeseman, J. A. Jr. Montgomery, T. Vreven, K. N. Kudin, J. C. Burant, J. M. Millam, S. S. Iyengar, J. Tomasi, V. Barone, B. Mennucci, M. Cossi, G. Scalmani, N. Rega, G. A. Petersson, H. Nakatsuji, M. Hada, M. Ehara, K. Toyota, R. Fukuda, J. Hasegawa, M. Ishida, T. Nakajima, Y. Honda, O. Kitao, H. Nakai, M. Klene, X. Li, J. E. Knox, H. P. Hratchian, J. B. Cross, V. Bakken, C. Adamo, J. Jaramillo, R. Gomperts, R. E. Stratmann, O. Yazyev, A. J. Austin, R. Cammi, C. Pomelli, J. W. Ochterski, P. Y. Ayala, K. Morokuma, G. A. Voth, P. Salvador, J. J. Dannenberg, V. G. Zakrzewski, S. Dapprich, A. D. Daniels, M. C. Strain, O. Farkas, D.

- K. Malick, A. D. Rabuck, K. Raghavachari, J. B. Foresman, J. V. Ortiz, Q. Cui, A. G. Baboul, S. Clifford, J. Cioslowski, B. B. Stefanov, G. Liu, A. Liashenko, P. Piskorz, I. Komaromi, R. L. Martin, D. J. Fox, T. Keith, M. A. Al-Laham, C. Y. Peng, A. Nanayakkara, M. Challacombe, P. M. W. Gill, B. Johnson, W. Chen, M. W. Wong, C. Gonzalez and J. A. Pople, *Gaussian 09*, revision D.01; Gaussian, Inc.: Wallingford, CT, 2009.
- 28 D. Frenkel and B. Smit, *Understanding molecular simulation: from algorithm to applications*; Academic Press, San Diego, 2nd ed., 2002.
- 29 M. P. Allen and D. J. Tildesley, *Computer Simulation of Liquids*; Clarendon: Oxford, 1987.
- 30 S. Plimpton, *J. Comput. Physics* 1995, **117**, 1-19.
- 31 J. C. Platteeuw and J. H. van-der Waals, *Molecular Physics* 1958, **1**, 91–96.
- 32 W. L. Jorgensen, D. S. Maxwell and J. Tirado-Rives, *J. Am. Chem. Soc.* 1996, **118**, 11225–11236.
- 33 (a) T. Kurtán, N. Nesnas, F. E. Koehn, Y.-Q. Li, K. Nakanishi, N. Berova, *J. Am. Chem. Soc.* 2001, **123**, 5974–5982; (b) A. G. Petrovic, G. Vantomme, Y. L. Negrón-Abril, E. Lubian, G. Saielli, I. Menegazzo, R. Cordero, G. Proni, K. Nakanishi, T. Carofiglio, N. Berova, *Chirality* 2011, **23**, 808–819; (c) S. Banala, R. G. Huber, T. Mueller, M. Fechtel, K. R. Liedl, B. Krauetler, *Chem. Comm.* 2012, **48**, 4359–4361.
- 34 T. Buchell and M. Rogers, *SAE Tech. Pap. Ser.* 2000, 2000-01-2205.
- 35 E. D. Sloan, *Nature* 2003, **426**, 353-359.
- 36 W. Wang, C. L. Bray, D. J. Adams and A. I. Cooper, *J. Am. Chem. Soc.* 2008, **130**, 11608-11609.

- 37 (a) G. Kresse and J. Furthmüller, *Comput. Mater. Sci.* 1996, **6**, 15-50; (b) G. Kresse and J. Furthmüller, *Phys. Rev. B* 1996, **54**, 11169-11186.
- 38 J. P. Perdew, K. Burke, and M. Ernzerhof, *Phys. Rev. Lett.* 1996, **77**, 3865-3868.
- 39 (a) P. E. Blöchl, *Phys. Rev. B* 1994, **50**, 17953-17979; (b) G. Kresse and D. Joubert, *Phys. Rev. B* 1999, **59**, 1758-1775.
- 40 H. J. Monkhorst and J. D. Pack, *Phys. Rev. B* 1976, **13**, 5188-5192.
- 41 S. Grimme, *J. Comp. Chem.* 2006, **27**, 1787-1799
- 42 S. Nosé, *J. Chem. Phys.* 1984, **81**, 511-519
- 43 (a) F. Labat, C. Pouchan, C. Adamo and G. E. Scuseria, *J. Comput. Chem.* 2011, **32**, 2177-2185; (b) J. Arago, J. C. Sancho-Garcia, E. Orti and D. Beljonne, *J. Chem. Theory Comput.* 2011, **7**, 2068-2077; (c) Y. Iwabata and H. Nakai, *Int. J. Quantum Chem.* 2015, **115**, 309-324.
- 44 Y. Tawada, T. Tsuneda, S. Yanagisawa, T. Yanai and K. Hirao, *J. Chem. Phys.* 2004, **120**, 8425.
- 45 (a) A. Szemik-Hojniak, K. Oberda, I. Deperasinska, Y. P. Nizhnik and L. Jerzykiewicz, *Polyhedron*, 2015, **88**, 190-198; (b) J. Mack, J. Stone and T. Nyokong, *J. Porphyrins Phthalocyanines* 2014, **18**, 630-641; (c) J. Mack, X. Liang, T. V. Dubinina, L. G. Tomilova, T. Nyokong and N. Kobayashi, *J. Porphyrins Phthalocyanines* 2013, **17**, 489-500.
- 46 S. Ma, D. Sun, J. M. Simmons, C. D. Collier, D. Yuan and H.-C. Zhou, *J. Am. Chem. Soc.* 2008, **130**, 1012-1016.
- 47 X.-S. Wang, S. Ma, K. Rauch, J. M. Simmons, D. Yuan, X. Wang, T. Yildirim, W. C. Cole, J. J. López, A. D. Meijere and H.-C. Zhou, *Chem. Mater.* 2008, **20**, 3145-3152.
- 48 H. Wu, W. Zhou and T. Yildirim, *J. Am. Chem. Soc.* 2009, **131**, 4995-5000.

49 J. Guan, X. Pan, X. Liu and X. Bao, *J. Phys. Chem. C* 2009, **113**, 21687-21692.

50 Y. Zhao, X. Liu and Y. Han, *RSC Adv.* 2015, **5**, 30310-30330.

### Table of Contents Graphic and Synopsis

A large variety of the conceptual three- and four-fold tetraazaporphyrin- and sutetraazaporphyrin-based functional 3D nanocage and nanobarrel structures have been proposed on the basis of *in silico* design. Stability of the  $O_h$  symmetry nanocages and  $D_{4h}$  symmetry nanobarrels were elucidated on the basis of DFT calculations while the optical properties were accessed using the TDDFT approach. It was shown that the electronic structures and vertical excitation energies of the functional nanocage and nanobarrel structures could be easily tuned up by their size, topology, and the presence of  $sp^3$  carbon atoms. Based on DFT and TDDFT calculations, the optical properties of the new materials can be rival to known quantum dots and superior to monomeric phthalocyanines and their analogues. MD simulations indicative that the most of proposed structures would exceed DOE target for methane gas storage.

